Combined Off-specular and Specular reflectometry: Elucidating the complex structure of soft buried interfaces

Aljoša Hafner,[a,b] Philipp Gutfreund,[a]* Boris P. Toperverg,[a,c] Andrew O.F. Jones,[b] Johann P. de Silva,[b] Andrew Wildes,[a] Henry E. Fischer,[a] Mark Geoghegan[d1] and Michele Sferrazza [b]*

[a]*Institut Laue - Langevin, 71 avenue des Martyrs, CS 20156, 38042 Grenoble, Cedex 9, France,* [b]*Université Libre de Bruxelles, Département de Physique, Boulevard du Triomphe, 1050 Brussels, Belgium,* [c]*Petersburg Nuclear Physics Institute, National Research Center "Kurchatov Institute", 188300 Gatchina, Russia, and* [d]*Department of Physics and Astronomy, University of Sheffield, Hicks Building, Hounsfield Road, Sheffield S3 7RH, United Kingdom. E-mail: gutfreund@ill.fr, msferraz@ulb.ac.be*

Abstract

Neutron specular reflectometry (SR) and off-specular scattering (OSS) are non-destructive techniques, which, through deuteration, give a high contrast even among chemically identical species and are therefore highly suitable for investigations of soft matter thin films. Through a combination of both techniques: the former yielding a density profile in the direction normal to the sample surface and the latter yielding a depth resolved in-plane lateral structure, one can obtain quite detailed information on

[1] Current address: School of Engineering, Newcastle University, Merz Court, Newcastle upon Tyne, NE1 7RU, UK

buried morphology on length scales ranging from $\sim$ Å to $\sim 10\,\mu$m. This is illustrated via quantitative evaluation of data on SR and OSS collected in time-of-flight (ToF) measurements of a set of films composed of immiscible polymer layers: protonated poly(methyl methacrylate) and deuterated polystyrene, undergoing a decomposition process upon annealing. Joint SR and OSS data analysis was performed by the use of a quick and robust originally developed algorithm including a common absolute scale normalization of both types of scattering, which are intricately linked, constraining the model to a high degree. This, particularly, makes it possible to readily distinguish between different dewetting scenarios driven by either the nucleation and growth of defects (holes, protrusions, etc.), or by thermal fluctuations of the buried interface between layers. Finally, the 2D OSS maps of particular cases are presented in different spaces and qualitative differences are explained, allowing to distinguish also qualitatively the in-plane structure of long-range order, correlated roughness and bulk defects by a simple inspection of the scattering maps prior to quantitative fits.

1. Introduction

Neutron reflectometry (NR), and X-ray reflectometry (XRR), are important techniques to probe condensed matter phases and, in particular, the properties of buried interfaces in thin films not easily accessible with other techniques. Each of these techniques has their own advantages. They can be applied in either specular and/or off-specular regimes, thus delivering either depth profiles of scattering length density (SLD) $\rho = Nb$, where N is number density and b is the scattering length, or probing SLD in-plane variation. It is important that real part b' of neutron scattering lengths $b = b' - b''$, which can be either positive or negative for different chemical elements or isotopes, and the imaginary part $b'' \geq 0$ are precisely measured and well tabulated for

almost all nuclei.[2] Therefore NR directly access *nuclear* number density distributions of reflecting materials, whereas X-rays probe the number density profiles of *electrons*, depending on the chemical composition.

Specular XRR and NR are nowadays well established techniques with routine application, ranging from magnetic (Zabel *et al.*, 2007) to soft matter (Daillant & Gibaud, 2009) and biological (Fragneto *et al.*, 2018) thin films and layered structures. Despite the substantially higher brilliance and flux of modern synchrotron sources of X-ray radiation, both techniques often deliver similar results. However, due to the ability to deuterate macromolecules (i.e. exchange hydrogen atoms with deuterium) and thus achieving a contrast even between chemically identical species, NR is especially useful for studying various soft matter systems (Penfold *et al.*, 1997). The other essential advantage of neutrons is their deep and non-destructive penetration into condensed matter, permitting to probe layers and interfaces deeply buried inside thick films or bulk materials. This is particularly useful for investigation of liquid-liqiud and liquid-air interfaces, as well as films freely floating at the surface, or displayed inside liquid environment (Jablin *et al.*, 2011). Such studies are possible due to the fact that the absorption length $l_{\mathrm{abs}} = (N\sigma_{\mathrm{abs}})^{-1}$, which is inversely proportional to the neutron absorption cross section $\sigma_{\mathrm{abs}} = b''^2$, is quite small for the vast majority of nuclei.[3]

The imaginary part b'' of the complex scattering length is usually a few orders of magnitude smaller than the modulus $|b'|$ of its real part b'. Therefore, for the case $b' > 0$ the extinction length of neutrons $l_{\mathrm{ext}} = 1/\sqrt{4\pi N b'}$ is commonly much smaller than the absorption length. Moreover, extinction and absorption lengths for neutrons are appreciably larger than their values for X-rays and hence probing inner interfaces well hidden from X-rays under relatively thick capping layers. It is also worth mentioning that most isotope scattering lengths of thermal and cold neutrons

[2] https://www.ncnr.nist.gov/resources/activation/
[3] https://www.ncnr.nist.gov/resources/activation/

are almost independent of the wavelength λ, whereas SLDs for X-rays are strongly wavelength dependent. This property of neutrons allows for an easier interpretation of the reflection coefficient $\mathcal{R}(q_z)$ dependence on the wave vector transfer component $q_z = (4\pi/\lambda)\sin\alpha_i$ normal to the surface, which is varied as a function of the incident angle α_i at fixed λ, or the wavelength λ at fixed α_i. The latter opportunity is realized in time-of-flight (ToF) reflectometry and is of particular convenience in the case of soft matter. Here we shall concentrate on the interpretation and quantitative description of ToF data in specular reflectivity (SR) and off-specular scattering (OSS) from solid polymer films undergoing dewetting.

Presently, there is a multitude of readily available software and established procedures for detailed analysis of the data on SR from different systems, taking into account their individual properties and constraints.[4] OSS arising due to lateral inhomogeneities may either appear as discrete peaks or as a continuous diffuse spectrum, depending on the shape, size, concentration and positions of inhomogeneities. The signal coming from fluctuations of interface positions commonly found in soft matter is usually of the diffuse type. The long-range lateral correlations of such fluctuations are of statistical origin, meaning that although a specific correlation length exists, the interface structure is not of a periodic type but rather exhibits a fractal-like shape in real space. However, in real experiments a well pronounced structure of diffuse scattering is often observed (see below) causing some difficulties in the quantitative data interpretation so that OSS is simply ignored. The other reason for underestimation of the role of OSS is usually ascribed to the limited neutron flux and limited detector efficiency. Meanwhile, both characteristics have been improved significantly in recent decades (Saerbeck *et al.*, 2018) and nowadays SR is routinely measured down to at least 6-7 orders of its magnitude. OSS, on the other hand, which is often simulta-

[4] http://www.reflectometry.net/reflect.htm#Analysis

neously recorded with position sensitive detectors (PSD), can be only 2-3 orders of magnitude smaller than the SR values and therefore it should not be neglected.

Qualitative interpretation and quantitative description of the OSS is more complex than that of SR, which is measured at the glancing angle of reflection $\alpha_f = \alpha_i$. With the latter constraint SR, $\mathcal{R}(q_z)$, is a 1D function of the single variable q_z and, hence, readily calculated with arbitrary accuracy for any reasonable SLD profile by optical considerations (Parratt, 1954; Heavens, 1960). In contrast, the OSS cross section is, by definition, determined at $\alpha_f \neq \alpha_i$ and, as we shall see, generally depends on at least three independent experimental variables: α_i, α_f and λ, but not on their unique combination q_z. Neither can the OSS cross section be generally presented as a function of the unique 3D wave vector transfer $\boldsymbol{q}$, as is usually the case in the Born Approximation (BA), or as a function of two 1D variables q_z and q_x, where the latter is the in-plane projection of the vector $\boldsymbol{q}$.

Although the neutron OSS cross section is relatively small, it is usually observed over the range where SR experiences total reflection. Within this range neutron OSS often becomes readily detectable receiving an appreciable interference enhancement (Yoneda, 1963), but cannot be treated in the BA. However, as a rule, it can be well described within the framework of the Distorted Wave Born Approximation (Mott & Massey, 1949; Newton, 2013) (DWBA) if the reference potential $U_0(\boldsymbol{r})$ is properly chosen: it should be sufficiently close to the true scattering potential $U(\boldsymbol{r})$, so that the deviation $\Delta U(\boldsymbol{r}) = U(\boldsymbol{r}) - U_0(\boldsymbol{r})$ can be treated as a perturbation delivering small corrections to the reference wave function which is *a priori* known for $U_0(\boldsymbol{r})$. The choice of the latter is quite obvious for the case of small self-affine roughness (Sinha *et al.*, 1988) or thermal surface fluctuations, such as capillary waves (Daillant & Belorgey, 1992). Then the reference potential is naturally chosen as an ideally flat surface providing optical distortions of incident neutron waves due to SR and refraction

due to the homogeneous optical potential U_0, while OSS generated by roughness-induced local deviations of the actual surface from its nominal position is taken into account in the first order of the perturbation theory. Later (Holý *et al.*, 1993; Holý & Baumbach, 1994; Tolan, 1998; Daillant & Gibaud, 2009), the DWBA was generalized for the case of X-ray OSS from rough interfaces in multilayered structures. Since then, DWBA equations derived for the model of *statistical roughness* were routinely employed to describe experimental data on OSS collected in a number of experiments on various systems.

However, statistical interface roughness is often neither a unique, nor dominating source of OSS. In many cases principle contribution to OSS is provided by other sources, such as: long range density, or concentration fluctuations (Lauter *et al.*, 2016; Lauter-Pasyuk *et al.*, 2003); magnetic, or structural micro-domains (Zabel *et al.*, 2007); natural, or artificial lateral micro-patterns (Toperverg & Zabel, 2015; Toperverg, 2015); dewetting holes (Castel *et al.*, 2020) etc., whenever corresponding SLD deviations from their mean value are sufficiently strong and of proper lateral and transverse dimensions. Although the DWBA approach can readily be formulated for all the cases listed above, when interpreting experimental OSS data one needs a reliable proof for the chosen model. Luckily, OSS is not arbitrarily normalized, but is firmly scaled by SR. This, as we shall see in the theoretical and illustrate in the experimental sections of the paper, strongly constrains the choice of the model for consequent fitting of SR and OSS data.

In the Theoretical section following the Introduction we formulate general principles of the DWBA based on coherence properties of neutron radiation in the case of *grazing incidence kinematics* and represent basic DWBA equations in the easy-to-program form avoiding numerical problems for thicker films. In view of that, we firstly reformulate algorithms for calculations of the SR amplitude and neutron wave field amplitudes

inside arbitrary SLD profiles approximated as a multilayer, or so called "box model". Special attention will be paid to establishing a proper relationship between SR and OSS. In particular, it shall be demonstrated that, contrary to the general belief that OSS carries not only the lateral structural information, OSS is heavily dependent on the neutron wave field distribution deduced from SR (Hafner, 2019). It is therefore important to devise a description which links the SR and OSS without any additional scaling parameters matching SR and OSS intensities and hence minimizing the amount of free parameters (Lauter *et al.*, 2016) to those solely referred to structure and distribution of lateral inhomogeneities.

In this paper we propose solutions to the aforementioned questions, by first describing a general workflow of OSS measurements, then qualitatively and quantitatively (using our own algorithm) discussing various features found in OSS spectra, and finally showing, how only using the combined SR and OSS information, a clear picture of the buried morphology can be obtained. In particular, it will be unambiguously shown that the main source of OSS recorded from immiscible polymer layers systems is not induced by solely interface roughening, but at certain stages of dewetting dominated by holes forming on the top surface and/or of protrusions of the layers.

2. Theoretical issues

In this section we first briefly describe kinematics of neutron scattering at grazing incidence, discuss general principles of SR and derive basic equations for SR amplitude and cross section. Then we consider general properties of SR and describe a version of Parratt's (Parratt, 1954) iterative routine used to calculate SR, as well as transmission and reflection amplitudes, for arbitrary 1D optical potentials approximated by a sequence of smooth layers with different SLDs. The algorithm presented below aims to avoid some numerical problems often occurring when the original form of the Parratt

formalism is applied to describe SR and OSS for sufficiently thick films. In parallel, we derive equations used to numerically calculate the neutron wave field propagating inside films and scattered in off-specular directions from lateral inhomogeneities. In the next subsection DWBA equations for scattering amplitude and cross section will be derived and thoroughly discussed for a set of particular examples relevant to problems of polymer film dewetting.

Although the here developed algorithm can be used for the analysis of grazing incidence small angle scattering (GISAS) measured with symmetric pin-hole collimation of the incident beam, we will mostly focus in the following on SR and OSS when scattered neutron flux is integrated over the in-plane direction perpendicular to the beam. Experimentally this corresponds to the case of a very asymmetric beam divergence, with a loose of this in-plane component and a highly collimated beam perpendicular to the sample plane as will be explained later. This is typically the case for neutron reflectometers, but not generally true for X-ray sources, especially on synchrotrons. Therefore we limit the discussion to neutrons in the following.

2.1. Wave functions at grazing incidence

The standard procedure of SR description assumes that the plane wave impinging from vacuum onto an ideally flat infinite surface at the glancing angle $\alpha_i = \alpha$ is totally, or partially reflected to the glancing angle $\alpha_f = \alpha$ and $\theta_y = 0$ as sketched in Fig. 1. In the latter case the wave is also partially refracted into the laterally homogeneous matter below the surface at the glancing angle $\alpha_{\rm refr}$. These statements constitute *Snell's law* which follows from two properties of the interaction potential $U(\boldsymbol{r}) = 2\pi\hbar^2 N b(\boldsymbol{r})/m$ where m is the neutron mass. The first of the properties is that interaction potential is *stationary* and does not allow any energy exchange between a neutron and the sample, hence conserving the length of the incident wave vector:

$|\boldsymbol{k}_f| = |\boldsymbol{k}_i| = k$, where $k = (2\pi/\lambda)$. The second property is that interaction potential $U(\boldsymbol{r}) = U(z)$ depends on solely the 1D coordinate z normal to the surface providing *translational invariance* of the medium with respect to its shift parallel to the surface plane. Such invariance conserves both in-plane projections, $k_i^x = k_f^x$ and $k_i^y = k_f^y$ of the incident wave vector $\boldsymbol{k}_f^{\|} = \boldsymbol{k}_i^{\|} = \boldsymbol{k}^{\|}$.

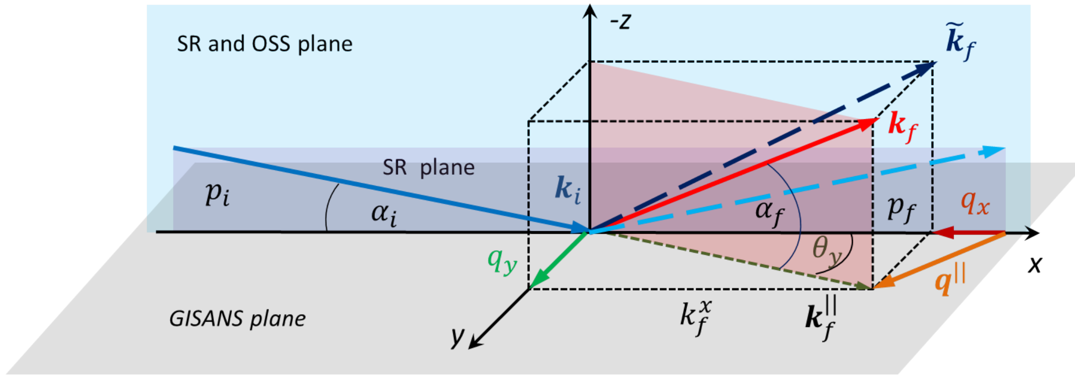

Fig. 1. Scattering kinematics at grazing incidence. The incoming wavevector is $\boldsymbol{k}_i$, and the outgoing wavevector is $\boldsymbol{k}_f$ with their in-plane components $\boldsymbol{k}_i^{\|}$ and $\boldsymbol{k}_f^{\|}$ and out-of-plane projections onto the $z-$ axis p_i and p_f, respectively. In the case of specular reflection, the incoming and outgoing glancing angles are equal $\alpha_i = \alpha_f$ and the in-plane angle $\theta_y = 0$ leading to both components q_x and q_y of the in-plane wavevector transfer $\boldsymbol{q}_{\|}$ turn to zero, while the out-of-plane component $q_z = 2p_i = 2p_f$. In the case of GISANS the angles $\alpha_f \neq \alpha_i$ and $\theta_y \neq 0$ lead to wavevector transfer components $q_x \neq 0$ and $q_y \neq 0$ contributing to the total in-plane wavevector transfer $\boldsymbol{q}_{\|}$. In the case of OSS the scattered flux is integrated over the angle θ_y and depends on incident, $\boldsymbol{k}_i$, and outgoing, $\tilde{\boldsymbol{k}}_f$ wavevectors with projections $p_i = \sin\alpha_i$, $p_f = \sin\alpha_f$ and $k_i^x \neq \tilde{k}_f^x$, where $k_i^x = k\cos\alpha_i$ and $\tilde{k}_f^x = k\cos\alpha_f$ with $\alpha_f \neq \alpha_i$.

This means that both in-plane projections q_x and q_y of the lateral wave vector transfer, $\boldsymbol{q}_{\|} = \boldsymbol{k}_f^{\|} - \boldsymbol{k}_i^{\|}$,

$$q_x = k(\cos\alpha_f \cos\theta_y - \cos\alpha_i), \quad (1)$$

$$q_y = k\cos\alpha_f \sin\theta_y, \quad (2)$$

turn to zero: $q_x = 0$ and $q_y = 0$. Solving this pair of equations one immediately obtains the Snell's law for SR: $\alpha_f = \alpha_i = \alpha$ and $\theta_y = 0$.

As a consequence, the normal component,

$$q_z = k(\sin\alpha_f + \sin\alpha_i), \tag{3}$$

of the wave vector transfer $\boldsymbol{q}$ at SR is equal to $q_z = p_i + p_f = 2p$, where $p = k\sin\alpha$, while $p_i = k\sin\alpha_i$ and $p_f = k\sin\alpha_f$ are normal projections of wave vectors $\boldsymbol{k}_i$ and $\boldsymbol{k}_f$. Note, that due to the truncation effect of the surface the translational symmetry of space with respect to a shift along the $z-$axis in Fig. 1 is violated and the neutron is able to transfer some momentum $\hbar q_z \neq 0$ (but not energy!) to the sample.

The in-plane translational invariance assumed in the above consideration is based on the continuous medium approximation which totally ignores an atomic structure. The latter, however, plays a role if the wave vector transfer is comparable with the reciprocal inter-atomic distances. This is not the case at shallow angles of incidence, $\alpha_i \ll 1$, and scattering, $\alpha_f \ll 1$, at which $q_x \approx (\pi/\lambda)(\alpha_i^2 - \alpha_f^2 - \theta_y^2)$, $q_y \approx (2\pi/\lambda)\theta_y$ and $q_z \approx (2\pi/\lambda)(\alpha_i + \alpha_f)$ are sufficiently small. Moreover, in this subsection we also neglect large scale surface and bulk inhomogeneities for the moment which dimensions may be comparable with the experimentally accessible range for the wave vector transfer components. Their contribution in OSS will be considered in the following subsections. Due to the *superposition principle*, the solution of the 3D wave equation with a 1D potential $U(z)$ can be factorized into the product: $\Psi_0(\boldsymbol{r}) = e^{i\boldsymbol{k}^{\parallel}\boldsymbol{r}^{\parallel}}\psi_0(z)$, where in empty space above the surface

$$\psi_0(z) = e^{ipz} + Re^{-ipz}. \tag{4}$$

Here the first term, $\psi_0^i(z) = e^{ipz}$, refers to the neutron wave propagating to the surface, while the second one, $\psi_0^f(z) = Re^{-ipz}$ corresponds to the wave reflected from the surface with the *reflection amplitude* $R = R(q_z)$. The latter is, generally, a complex function of only the normal component $q_z = 2p$ of the 3D wave vector $\boldsymbol{q}$.

Strictly speaking, incident and reflected waves functions,

$$\Psi_0^i(\boldsymbol{r}) = e^{i\boldsymbol{k}^{\parallel}\boldsymbol{r}^{\parallel}}\psi_0^i(z) \quad \text{and} \quad \Psi_0^f(\boldsymbol{r}) = Re^{i\boldsymbol{k}^{\parallel}\boldsymbol{r}^{\parallel}}\psi_0^f(z), \tag{5}$$

describe free wave propagation at $z \leq 0$, i.e. in upper hemisphere, but in different asymptotic regimes. The first equation is valid in the limit $\boldsymbol{r}^{\parallel} \to -\infty$, while the second one corresponds to the outgoing wave in the limit $\boldsymbol{r}^{\parallel} \to +\infty$. This silently assumes that the front of the incident plane wave is not infinite and restricted by a finite entrance diaphragm excluding interference between incident and reflected waves at macroscopically large distances from the surface.

Alternatively, in the immediate vicinity above the surface, both waves are simultaneously present if the wave function is written in Eq.(4) as a superposition of both waves: $\psi_0(z) = \psi_0^i(z) + \psi_0^f(z)$. Although equation Eq.(4) is replicated in a number of text books, it is worth noting that the co-existence of the reflected and incident neutron waves may, at first sight, contradict the normalization of the neutron wave function. Indeed, in the *interference zone* just above the surface the wave field amplitude $\psi_0(z) \approx (1 + R)$. But at the threshold of total reflection $R \approx 1$, and then $\psi_0(z) \approx 2$, whereas $|\psi_0^i| = |\psi_0(-\infty)| = 1$.

2.2. Fresnel equations

The controversy concerning Eq. (4) can be illustrated for the simplest example of SR from semi-infinite homogeneous media separated from the vacuum by an ideally sharp and flat surface. Then the explicit expression for the reflection amplitude can be readily obtained taking into account that a fraction of the incident wave may be also refracted into the media. Below the surface its propagation is described by the plane wave,

$$\psi_s(z) = Te^{ip_s z}, \tag{6}$$

with the *transmission amplitude* $T = T(q_z)$ and the refracted wave number $p_s = \sqrt{p^2 - p_c^2}$, which depends on the critical wave number $p_c = 2\sqrt{\pi\rho}$ of total reflection.

Then conditions for the neutron *flux continuity* through the surface immediately yield a pair of equations:

$$1 + R = T \quad \text{and} \quad p(1 - R) = p_s T, \tag{7}$$

while their solution delivers Fresnel equations for the reflection and transmission amplitudes:

$$R = \frac{p - p_s}{p + p_s} \quad \text{and} \quad T = \frac{2p}{p + p_s}. \tag{8}$$

From the first equation it follows that the reflection amplitude $R(p)$ is a real function of p for positive and purely real SLD. At $p > p_c$ it asymptotically decays as p^{-2} in the limit $p \gg p_c$. Therefore, over the range $p > p_c$ the reflected wave is exactly in-phase with the incident one at $z = 0$, and the sum of their amplitude $1 + R > 1$, approaching 1 at $p \gg p_c$ when the reflection amplitude approaches zero. If, in contrast, p tends to the critical edge the reflection amplitude increases reaching the value $R(p_c) = 1$, where its first derivative diverges as $(p - p_c)^{-1/2}$. Then the wave field intensity $|\psi_0^i(z) + \psi_0^f(z)|^2 = 4$ at $z = 0$ and $p = p_c$, while oscillating as a function of z at fixed $p > p_c$ and vice versa.

Within the same range $p > p_c$ the transmission amplitude $T(p)$ is also a real function of p approaching the asymptotic value $T = 1$ at $p \gg p_c$, but increasing up to the value $T(p_c) = 2$ and revealing the same type of threshold singularity as $R(p_c) = 2$. Hence, at $p \to p_c$ the wave field intensity $|\psi_t(z)|^2$ also increases by the factor four at $p = p_c$, where its wave number p_s turns to zero and the neutron field becomes homogeneously distributed everywhere in the matter below the surface.

Over the interval $0 < p < p_c$ the reflection amplitude $R = |R|e^{i\chi_r}$ becomes a complex function of p with the absolute value $|R| = 1$ and the phase χ_r is negative

monotonically increasing from $\chi_r = -\pi$ at $p = 0$ up to $\chi_r = 0$ at $p \geq p_c$. In the same interval the transmission amplitude $T = |T|e^{i\chi_t}$ is also a complex function of p. Its absolute value, $|T|$, linearly approaches zero at $p = 0$, while monotonically increasing up to $|T| = 2$ at $p = p_c$, where it reveals a cusp like maximum, approaching asymptotic value $|T| = 1$ at $p \gg p_c$. The phase χ_t turns to zero in either of the two limits $p \to 0$ and $p \gg p_c$ reaching a minimum value $\chi_t = -\pi/4$ at $p = p_c/2$.

Below the critical edge the refracted neutron field is often called a *evanescent wave*, although it just exponentially decays into depth of material, but with no in-plane propagation as follows from the consideration in the next sub-section.

2.3. Interference and flux conservation

In order to resolve possible confusion with the fact that the wave field intensity may exceed that of the incident wave it is important to emphasize that the enhancement of the transmission coefficient e.g. up to a value $|T|^2 = 4$ is a direct consequence of the constructive interference between incident and reflected waves at $p > p_c$ where both waves are perfectly in-phase, while at $p = p_c$ their amplitudes equal 1. As a result, above the surface the wave field intensity oscillates so that $|\psi(z)|^2 = 4\cos^2\varphi_c(z)$, where $\varphi_c(z) = p_c z$ is the phase of the wave function at $p = p_c$. Below the surface the wave field intensity $|\psi(z)|^2 = 2(p/p_c)\exp(-\frac{1}{2}|p_s|z)$ exponentially decays with depth of the reflecting material over the whole range $p < p_c$ reaching its maximum value $|\psi(p_c)|^2 = 4$ independent of z at $p = p_c$. As we shall see, the enhancement of the wave field intensity, or probability density, is visualized in the Yoneda (Yoneda, 1963) effect in OSS discussed below.

The fact that the wave field amplitudes in Eqs.(4,6) may exceed 1 does not, contradict to the normalization of wave functions if one considers the *probability current*, or flux density $\boldsymbol{j}(\boldsymbol{r})$, but not the probability $|\Psi(\boldsymbol{r})|^2$ itself. Indeed, the flux density is

defined as a vector,

$$\boldsymbol{j}(\boldsymbol{r}) = \frac{i\hbar}{2m} \lim_{\boldsymbol{r}\to\boldsymbol{r}'} \left\{ \Psi(\boldsymbol{r})[\nabla'\Psi^*(\boldsymbol{r}')] - [\nabla\Psi(\boldsymbol{r})]\Psi^*(\boldsymbol{r}') \right\}, \tag{9}$$

which tangential component $\boldsymbol{j}^{\parallel} = \boldsymbol{v}^{\parallel}$ is just equal to the corresponding component of the neutron velocity vector $\boldsymbol{v} = \hbar\boldsymbol{k}/m$ and is conserved either above, or below the surface. At the same time, its normal component incident onto the surface is equal to: $j_z^r = v_z$, while the reflected one, $j_z = -v_z|R|^2$, has opposite sign of the velocity component $v_z = \hbar p_0/m$. Substituting Eq.(6) into Eq.(9) one can obtain the equation for the flux density $j_z^t = v_z^t|T|^2\exp(-2p''z)$ of neutrons propagating below the surface with velocity $v_z^t = \hbar p'/m$ proportional to the real part of the complex wave number p, and exponentially decaying with depth of the material with the rate proportional to its imaginary part p''.

Integrating reflected and transmitted flux over corresponding beam cross sections and normalizing their sum to total incident flux one can readily formulate the total flux conservation law as follows:

$$|R|^2 + (p'_s/p)|T|^2 e^{-2p''_s z} = 1. \tag{10}$$

This equation formally agrees with the Fresnel Eqs.(8). For purely real SLD the second term in Eq.(10), describing the contribution of the transmitted beam vanishes at $p \leq p_c$, while $|R|^2 = 1$. This means that although the neutron field below the critical edge edge tunnels into the medium for a distance in the order of the extinction length $l_{\text{ext}} = p^{-1}$ it does not propagate along the surface, being totally reflected into the upper hemisphere. Above the critical edge, i.e. at $p_0 \geq p_c$, both reflected and refracted waves contribute to the total flux conservation so that $|R|^2 + (p_s/p)|T|^2 = 1$.

In the case of a non-zero imaginary part of the SLD the difference between the right and left hand sides of Eq.(10) determines the absorption coefficient K_a. The latter, as well as reflection and transmission coefficients, crucially depend on e.g. the

SLD profile. Regretfully, analytical solutions of the wave equation are know only for a very few examples of SLD depth profiles. However, by stratification, numerically exact solutions for SR can be obtained for arbitrary 1D SLD distributions by the use of readily available software.[5] In the following one of the most popular algorithms of such calculations is discussed in view of its further application in the calculations of OSS.

2.4. Distorted waves in layered structures, Parratt formalism

The algorithm of calculations of reflection and transmission amplitudes, as well as neutron wave field distribution within an arbitrary SLD profile, is based on the approximation of the SLD depth profile $\rho(z)$ by a histogram corresponding to a sequence of N homogeneous layers as depicted in Fig.2.

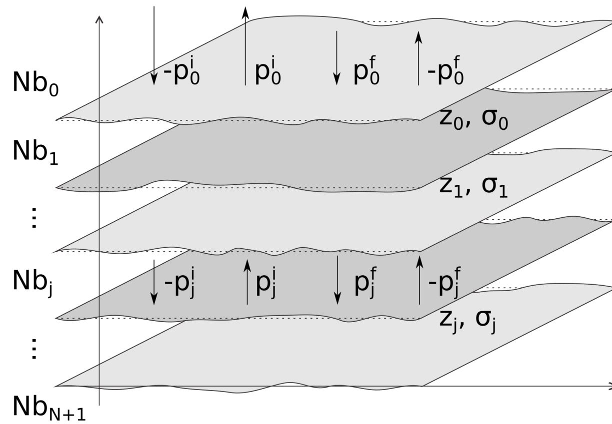

Fig. 2. Schematic of a multilayer sample stratified into N layers (n=1,..,N) along the z-axis with scattering length densities (SLDs) Nb_n and interface roughness σ_n at positions z_n, sandwiched between the top phase (SLD=Nb_0) and bottom phase (SLD=Nb_{N+1}). The wave vector projections on the z-axis p_n are noted for the incoming (i) and outgoing (f) waves schematically shown as downwards and upwards traveling to signify the physical meaning of the 16 combination of the transverse scattering form factor calculated later.

[5] http://www.reflectometry.net/reflect.htm#Analysis

Hence, the SLD of the film:

$$\rho(z) = \sum_{l=1}^{N} \rho_l(z), \tag{11}$$

is represented to arbitrary precision as a Riemann sum over layer SLDs $\rho_l(z) = \overline{\rho}_l$ which are constant for $z_{l-1} \leq z < z_l$. This constant, $\overline{\rho}_l$, can be chosen as the mean SLD value,

$$\overline{\rho}_l = \frac{1}{d_l} \int_{z_{l-1}}^{z_l} dz \rho(z), \tag{12}$$

averaged over the lth layer thickness $d_l = z_l - z_{l-1}$.

At $z \leq z_0$, where $z_0 = 0$, i.e. above the film front face of the layer stack, $\rho(z) = \overline{\rho}_0$ is the SLD of the front phase, e.g. air, while at $z \geq z_{N+1}$ the SLD $\rho(z) = \overline{\rho}_{N+1} = \rho$ corresponds to the SLD of the sub-phase, e.g a homogeneous substrate.

The wave function $\psi(z)$ of the neutron propagating through such a system is also written as a Riemann sum of plane waves:

$$\psi(z) = \sum_{l=1}^{N} \left(t_l e^{ip_l(z-z_{l-1})} + r_l e^{-ip_l(z-z_{l-1})} \right) \tag{13}$$

where $t_l = t_l(p_l)$ and $r_l = r_l(p_l)$ are amplitudes of transmission into the lth layer and, respectively, reflection from its back interface. Both amplitudes are defined within the segments $z_{l-1} \leq z < z_l$ as complex functions of the complex wave numbers $p_l = (p^2 - p_{lc}^2)^{1/2}$ depending on the critical wave numbers $p_{lc} = 2\sqrt{\pi \overline{\rho}_l}$ of total reflection. In the upper phase, e.g. air, above the front face of the multilayer, $\psi(z) = \psi_0(z)$ is given in Eq.(4), while in the sub-phase, e.g. substrate, $\psi(z) = \psi_t(z)$ is determined by Eq.(6).

Taking into account the neutron flux continuity through each interface one can write down the following system of coupled pairs of equations:

$$e^{i\varphi_l} t_l + e^{-i\varphi_l} r_l = t_{l+1} + r_{l+1}\,, \tag{14}$$

$$p_l \left(e^{i\varphi_l} t_l - e^{-i\varphi_l} r_l \right) = p_{l+1} \left(t_{l+1} - r_{l+1} \right)\,, \tag{15}$$

in which at $0 < l \leq N$ complex phases $\varphi_l = p_l d_l$ are gained by the neutron wave traveling through the lth layer, while in accordance with Eqs.(4,6) $t_0 = 1$, $r_0 = R$, $t_{N+1} = T$, and $r_{N+1} = 0$. This system contains $2(N+1)$ linear equations with respect to $2(N+1)$ transmission and reflection amplitudes, including R and T. Therefore it can be readily solved by methods of linear algebra, e.g. by means of a recursion procedure known as the Parratt formalism (Parratt, 1954). Applied to the ratio $R_l = r_l/t_l$ this yields:

$$R_l = \frac{r^F_{l,l+1} + R_{l+1}}{1 + r^F_{l,l+1} R_{l+1}} e^{2i\varphi_l} \tag{16}$$

with the Fresnel amplitudes of reflection,

$$r^F_{l,l+1} = \frac{p_l - p_{l+1}}{p_l + p_{l+1}}, \tag{17}$$

from the interface between the lth and $(l+1)^{\text{st}}$ layers.

Taking further into account that $r_{N+1} = R_{N+1} = 0$, from Eq.(16) one immediately receives the explicit expression: $R_N = r^F_{N,N+1} \exp(2i\varphi_N)$ for the normalized reflection amplitude R_N. Then, substituting it back into Eq.(16) yields the expression for R_{N-1}, and so on, until the iteration procedure delivers equations for all amplitudes R_l, and finally, for the reflection amplitude $R = R_0$ of the whole multilayer.

In parallel, one can readily derive a recursion equation for transmission amplitudes in Eq.(13):

$$t_{l+1} = e^{i\varphi_l} \frac{t^F_{l,l+1} t_l}{1 + r^F_{l,l+1} R_{l+1}}, \tag{18}$$

which uses the same denominator as Eq.(16), and the Fresnel transmission amplitudes:

$$t^F_{l,l+1} = \frac{2p_l}{p_l + p_{l+1}}\,. \tag{19}$$

Finally, one can also calculate the array of reflection amplitudes $r_l = R_l t_l$ and the wave field intensity $|\psi(p_0, z)|^2$ as a function of the wave number p_0 at depth z. Note that Eqs.(16–19) contain exponential factors. At $p_l \geq p_{lc}$ they oscillate with frequencies

inversely proportional to layer thicknesses due to real parts φ_l' of phases φ_l generating thickness oscillations, or Kiessig fringes, on the reflectivity curve and quite a complicated interference pattern of the wave filed distribution displayed in Fig. 3.

At the same time, the imaginary parts of the phases φ_l'' may become rather large below the critical edge of total reflection from sufficiently thick layers. This does not cause any numerical problem for computation of the amplitudes t_l and r_l, as in our version of the recursive procedure the imaginary parts φ_l'' are always positive and hence exponential factors in Eqs.(16–18) may become small, but never large. In contrast, numerical problems may emerge while computing wave functions in Eq.(13). In this case exponentially small reflection amplitudes r_l are multiplied by exponential factors which may simultaneously become huge due to negative imaginary parts of phases $-p_l(z - z_{l-1})$ of reflected waves. The resulting products are, in reality, neither exceptionally small or large, but may cause numerical instability due to the lost accuracy at their multiplication.

The numerical problem outlined here is quite relevant for the particular cases discusses below, as our systems are commonly composed of relatively thick layers with high (deuterated) SLDs. The problem can be easily solved via redefinition of the reflection amplitudes $r_l = e^{i\varphi_l}\widetilde{r}_l$ via the auxiliary amplitude $\widetilde{r}_l$. Then instead of Eq.(13) the wave function is determined by the equation:

$$\psi(z) = \sum_{l=1}^{N+1} \left(t_l e^{ip_l(z-z_{l-1})} + \widetilde{r}_l e^{i(\varphi_l - p_l(z-z_{l-1}))} \right) , \tag{20}$$

where $\widetilde{r}_l = \widetilde{R}_l t_l$, $z_{l-1} < z \leq z_l$ and the auxiliary function,

$$\widetilde{R}_l = \frac{r^F_{l,l+1} + R_{l+1}}{1 + r^F_{l,l+1} R_{l+1}} e^{i\varphi_l} , \tag{21}$$

is expressed via the already computed numerator and denominator arrays.

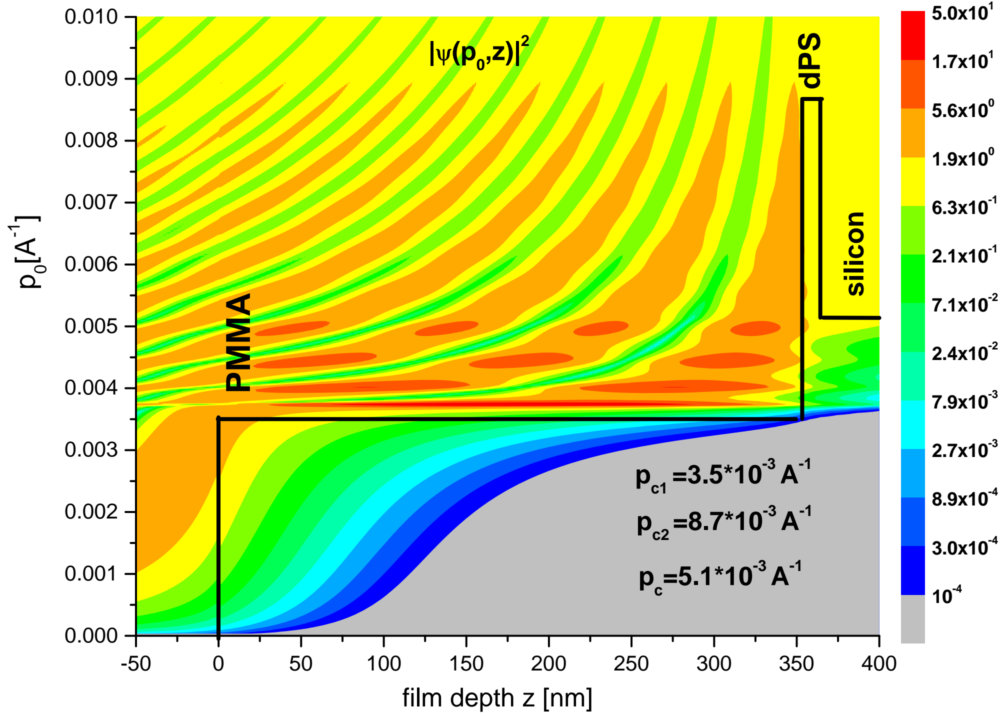

Fig. 3. Wave field $|\psi(p,z)|^2$ distribution over wave numbers $p_0 = p$ and depth z inside, above and below the h-PMMA/d-PS polymer bilayer on a silicon wafer plotted along with the SLD profile histogram.

An example of the wave field distribution $|\psi(p,z)|^2$ calculated in accordance with Eq.(20) for a hydrogenated poly(methyl-methacrylate)/deuterated polystyrene (h-PMMA/d-PS) polymer bilayer on a silicon substrate, plotted in Fig. 3 shows a feature-rich picture. Indeed, above the surface, i.e. at $z < 0$, the wave field with high incident wave numbers p_0 rapidly oscillates with a frequency matching the thickness $d_1 = 350\,\text{nm}$ of the top h-PMMA layer with a low SLD and a critical wave number $p_{c1} = 3.5 \times 10^{-3}\text{Å}^{-1}$. However, within the range $p_{c1} < p < p_{c2}$, lower than the critical value $p_{c2} = 8.7 \times 10^{-3}\text{Å}^{-1}$ of the deuterated 10 nm thick d-PS layer, oscillations above the surface become distorted due to interference between incident and reflected waves. Finally, below p_{c1} the neutron wave intensity above the surface is enhanced by

a factor 4 revealing almost the same behavior as discussed above for total reflection from semi-infinite matter: in this range the neutron wave with $p_0 < p_{c1}$ exponentially decays into the thick PMMA layer reaching its back interface. However, the most interesting effect is seen within the top layer in the range $p_{c1} < p < p_c$, with the critical wave number for silicon $p_c = 5.1 \times 10^{-3}\text{Å}^{-1}$. In this range the waves refracted into the PMMA layer by tunneling though the d-PS barrier strongly interfere with the wave reflected from the Si substrate. Such interference results in a dramatic, up to 2 orders of magnitude, enhancement of the neutron wave intensity inside the top layer. This effect looks similar to that observed (Wolff *et al.*, 2019) in a resonance well potential and used to enhance the sensitivity to incoherent neutron scattering from hydrogen contained in a thick vanadium layer sandwiched between two iron layers. In the following section this effect is used to enhance OSS from inhomogeneities in polymer layers during dewetting.

2.5. Bulk defects and interface roughness

Although the algorithm described above can be, in principle, used for arbitrary SLD profiles formally approximated by a sequence of sufficiently thin homogeneous slabs, the practical choice of those slabs is often determined by real interfaces separating layers with different SLDs. In many cases real interfaces are not perfect, but reveal some roughness, while real physical layers are not perfectly homogeneous, but may contain various kinds of "bulk defects" due to e.g. frozen thermal fluctuations, structural domains, inclusions of foreign phases and other imperfections. However, a well collimated and monochromatic neutron wave impinging onto a macroscopically flat film at shallow angles almost totally averages out scattering in all directions except for that of specular reflection and refraction. If the latter optical effects overwhelm any scattering from defects, then the optical considerations above apply providing

exact solutions for the SLD profile represented by the same Eq.(11) in which $\rho(z)$ is substituted by the mean SLD $\overline{\rho}(z) = \langle \rho(\boldsymbol{r}_\parallel, z) \rangle$ averaged over the lateral coordinate $\boldsymbol{r}_\parallel$, while the SLD of the layer $\overline{\rho}_l$ in Eq.(12) denotes the mean SLD averaged over the layer volume.

In the case of sufficiently thick layers two types of imperfections can be distinguished already via the analysis of SR, i.e. those are homogeneously distributed over the entire layer depth, or concentrated at the interfaces. In the former case of "bulk defects" the mean SLD of the layer $\overline{\rho}_l$ does not coincide with the nominal value, often quantifiable by positions of critical edges of total reflection, or deduced from the fit of SR to the theoretical model. In contrast, interface imperfections such as roughness, surface waves, etc., do not modify the SLD of layers, but suppress interference fringes and decrease the reflectivity at high q_z. Such a classification of defects assumes that there exists two different length scales: the larger one determined by the layer thicknesses d_l over which laterally averaged the mean SLD $\overline{\rho}(z) = \overline{\rho}_l$ is essentially constant, and the smaller one, $\sigma_l \ll d_l$, ascribed to the lth interface widths between neighboring l^{th} and $(l+1)^{\text{st}}$ layers, and which is due to the fluctuation of the true interface position. The latter, $z_l(\boldsymbol{r}_\parallel)$, depends on the lateral projection x and y at a given lateral radius-vector $\boldsymbol{r}_\parallel$, and separates materials with SLD ρ_{l+1} above the interface at $z > z_l(\boldsymbol{r}_\parallel)$ from those with SLD ρ_l at $z \leq z_l(\boldsymbol{r}_\parallel)$ below the lth interface.

Assuming that $z_{l-1}(\boldsymbol{r}_\parallel) < z_l(\boldsymbol{r}_\parallel) < z_{l+1}(\boldsymbol{r}_\parallel)$, i.e. that neighboring interfaces never cross, one can separate the actual interface coordinate into two parts: $z_l(\boldsymbol{r}_\parallel) = \overline{z}_l + h_l(\boldsymbol{r}_\parallel)$, where $\overline{z}_l = \langle z_l(\boldsymbol{r}_\parallel) \rangle$ is the laterally averaged interface coordinate and $h_l(\boldsymbol{r}_\parallel)$ denotes the deviation of the true interface position from its mean value $\overline{z}_l$, determined by the equation $\langle h_l(\boldsymbol{r}_\parallel) \rangle = 0$. Then the root mean square (r.m.s.) value $\sigma_l = \sqrt{\langle h_l^2(\boldsymbol{r}_\parallel) \rangle}$ can be attributed to the effective width of the lth interface. Usually, it is assumed that height fluctuations $h_l(\boldsymbol{r}_\parallel)$ are randomly distributed in accordance with the normal law

with dispersion σ_l. In this case the mean SLD profile $\overline{\rho}_l(h_l) = \langle \rho_l(\boldsymbol{r}_\parallel, h_l) \rangle$ through the interface is described by the equation:

$$\overline{\rho}_l(h_l) = \frac{\rho_l + \rho_{l+1}}{2} + \frac{\rho_l - \rho_{l+1}}{2} \mathrm{erf}(h_l/\sqrt{2}\sigma_l), \tag{22}$$

via the Gauss error function and the corresponding SLDs ρ_{l-1} and ρ_l in the bulk of neighboring layers.

Unfortunately, no analytical solution for such a SLD profile is available. Therefore, alternative approximated solutions are proposed (see discussion in (Tolan, 1998)). One of them is based on the representation of the SLD profile in the interface region via the histogram, as described above. The other and more popular approach assumes (Nevot & Croce, 1980) that the result of interface smearing can be described introducing Debye-Waller (DW) like factors: $\exp(-2p_l p_{l+1}\sigma_l^2)$ for the Fresnel reflection amplitude $r^F_{l,l+1}$, and $\exp\{-(p_l - p_{l+1})^2\sigma_l^2/2\}$ for the Fresnel transmission amplitudes $t^F_{l,l+1}$ in Eqs.(16,18). Surprisingly, such a simple ansatz describes the behavior expected for reflection and transmission amplitudes not only qualitatively, but often provides an excellent description of experimentally measured neutron reflectivities with a set of reasonable values for σ_l used as fitting parameters. This fact, however, cannot unambiguously prove a validity of the ansatz, and e.g. guarantee that DW factors extracted from the fit are equal to those in Eq.(22).

Indeed, the Fresnel equations, as well as the Parratt formalism, are formulated for ideally sharp interfaces separating materials with homogeneous SLDs. Only then the solution of the wave equation can be represented in the form of Eqs.(13,20), or Eqs.(4,6). If, on the other hand, the SLD smoothly varies within some range $h_l \sim \sigma_l$ of the interface, then the wave function should also be continuous over this range along with its first and second derivatives. However, the second derivative of solutions in Eqs.(13,20), or Eqs.(4,6) are not continuous and, strictly speaking, cannot be used for gradual interfaces with the smearing $\sigma_l \sim p_0^{-1}$, while in the limit $\sigma_l p_0 \geq 1$ the quasi-

classical, or Wentzel-Kramers-Brrillouin (WKB) approach (Landau & Lifshitz, 1989) applies. In practice, this limit can hardly be accessed with NR, while most data on e.g. OSS are usually collected over the range close to the critical edges of total reflection $p_0 \sim p_{cl}$. There the SLD smearing plays a minor role in the wave function behavior and the solution for sharp interfaces, as we shall see, can be used for a rather precise description of OSS.

2.6. Cross section of specular reflection

All considerations above, as well as Eq.(10), actually, assume that the footprint of the incident beam at the surface is smaller than the surface area S_0, i.e. the sample is under-illuminated. Then the differential cross sections of SR can be defined as:

$$\left(\frac{d\sigma}{d\Omega}\right)_{\mathrm{SR}} = S_{\mathrm{SR}}(\alpha_i)|R(q_z)|^2\delta(\alpha_i - \alpha_f)\delta(\theta_y), \tag{23}$$

where the area $S_{\mathrm{SR}} = S_{\mathrm{SR}}(\alpha_i)$ is equal to the incident beam cross section S_b, so that the total cross section of SR integrated over the solid angle is: $\sigma_R^{\mathrm{tot}} = S_b|R|^2$. At sufficiently low incident angles $\alpha_i = \alpha_f$, however, the sample may become over-illuminated. Then a part of the incident beam bypasses the sample and the visible area of the sample surface $S_{\mathrm{SR}}(\alpha_i)$ is smaller than S_b. As a result, the sum in the right hand side of Eq.(10) is equal to the illumination factor $\Phi_{\mathrm{SR}}(\alpha_i) = S_{\mathrm{SR}}(\alpha_i)/S_b \leq 1$. In view of that, it is convenient to introduce instead of the SR cross section in Eq.(23) a dimensionless ratio $I_{\mathrm{SR}} = I_{\mathrm{SR}}(\alpha_i - \alpha_f, \theta_y)$ of the SR cross section normalized to the area S_b:

$$I_{\mathrm{SR}} = \Phi_{\mathrm{SR}}(\alpha_i)|R(q_z)|^2\delta(\alpha_i - \alpha_f)\delta(\theta_y), \tag{24}$$

for which the integral over over angles α_f and θ_y is the probability of SR at a given incident angle and wavelength. The pre-factor $\Phi_{\mathrm{SR}}(\alpha_i)$ can be calculated for any line shape of the surface frame and of the incident beam footprint. In the simplest case of rectangular shape, $\Phi_{\mathrm{SR}}(\alpha_i)$ is determined by a single parameter: the crossover angle

of total illumination α_0, which obeys the equation $\sin\alpha_0 = S_b/S_0$. Then $\Phi_{\rm SR}(\alpha_i) = \sin\alpha_i/\sin\alpha_0$ if $\alpha_i < \alpha_0$, while $\Phi_{\rm SR}(\alpha_i) = 1$ when $\alpha_i \geq \alpha_0$. In the case of $\alpha_0 > \alpha_c$, instead of the plateau of total reflection at $\alpha_i < \alpha_c$ one observes a linear increase of SR for monochromatic measurements which reaches a maximum value at $\alpha_0 = \alpha_c$ and then decreases again.

It is usually argued that one of advantages of the ToF mode in reflectometry, e.g. used in the present study, is that, in contrast to angular dispersive mode, it does not require precise knowledge of the illumination factor. This is partially true, as in ToF mode SR is measured as a function of the wavelength λ at a fixed incident angle, so that $\Phi_{\rm SR}(\alpha)$ is just a normalization constant. In addition, usually the sample is under-illuminated in ToF mode, making $\Phi_{\rm SR}(\alpha) = 1$. In any case, absolute normalization of the SR cross section becomes important when it is measured simultaneously with the OSS, as the illumination factor differs from that of SR. Moreover, due to the presence of OSS, part of the neutron flux is lost from the SR and transmission channels. Such losses are usually small and can be, if necessary, taken into account in the second order of the DWBA via the optical theorem (Toperverg *et al.*, 2000), resulting in an additional contribution to the imaginary part of the SLD. On the contrary, Eq.(10) regulates only the redistribution between reflected and transmitted parts of neutron flux formalizing the basic "sum rule". This rule should be satisfied for an arbitrary homogeneous 1D SLD distribution across the film body, if both SR reflection $|R|^2$ and transmission $|T|^2$ are measured and computed. One of the most popular algorithms for doing so delivers not only the reflection, but simultaneously the transmission amplitude, as well as the wave field distribution inside the film as is described in the previous subsection.

2.7. Resolution and coherence

Before discussing OSS in detail it is important to mention that the SR consideration above is essentially based on the concept of an ideal plane wave interacting with an ideally flat infinite surface. Therefore, Eq.(23) is, rigorously speaking, valid in the limit of $S_0 \to \infty$ and $S_b \to \infty$. On the other hand, it was assumed that the front of the incident wave is limited in area, e.g. by being framed by an entrance diaphragm. Such a diaphragm is set as close as possible to the sample and is should be sufficiently wide to transmit sufficient neutron flux and to minimize a possible contribution from Fraunhofer diffraction on the diaphragm and/or sample edges. Simultaneously, it should be narrow enough to avoid the above mentioned interference between incident and reflected waves while minimizing over-illumination of the sample. In principle, one can readily find a compromise between these mutually contradictory requirements.

On the other hand, the main assumption on the perfect coherence of neutron radiation is quite far from reality: neutrons are created within the macroscopically sized moderator in random moments of time and propagate in free space as spherical waves diverging from random points in the source volume. Nonetheless, on the long flight path to the sample fronts of these waves become substantially flattened. A sequence of diaphragms, or slits placed on this path selects the wave propagation direction, and hence angles of incidence α_i distributed around their nominal value $\overline{\alpha}_i$ with uncertainty δ_i depending on slit dimensions and distances between them. Similarly, the direction of scattering α_f is determined as $\overline{\alpha}_f$ with a spread δ_f depending on the detector acceptance, e.g. the cell size of a position-sensitive detector (PSD), and the sample-to-detector distance. In addition, the in-plane scattering angle θ_y is distributed around its nominal value $\overline{\theta}_y$ with (usually large) uncertainty δ_y. Last but not least, a spread δ_λ in the wavelength distribution around its mean value $\overline{\lambda}$ depending on the monochromator properties, or chopper system in ToF mode discriminating neutrons

over their wavelengths λ, determines the absolute values $k = k_i = k_f$ of the wave vectors.

All these uncertainties are taken into account via convolution of the SR cross section in Eq.(23) with the resolution function $W = W(\overline{\alpha}_i - \alpha_i, \overline{\alpha}_f - \alpha_f, \overline{\theta}_y - \theta_y, \overline{\lambda} - \lambda)$ of four independent variables, so that experimental data on SR can be compared with the SR cross section plotted as a function of any pair of variables, e.g. $\overline{\alpha}_i$ and $\overline{\alpha}_f$ at fixed $\overline{\lambda}$ and integrated over $\overline{\theta_y}$, or $\overline{\alpha}_f$ and $\overline{\lambda}$ at fixed $\overline{\alpha}_i$ in the ToF mode.

Such convolution can be readily accomplished assuming that the resolution function is factorized into the product: $W = W_i W_f W_y W_\lambda$, where $W_{i(f)} = W_{i(f)}(\overline{\alpha}_{i(f)} - \alpha_{i(f)})$, $W_y = W_y(\overline{\theta}_y - \theta_y)$, and $W_\lambda = W_\lambda(\overline{\lambda} - \lambda)$. Then the normalized reflected neutron flux is represented as a product, $I_{\rm SR} = W_y(\overline{\theta}_y)\overline{I}_{\rm SR}$, of two functions: $W_y(\overline{\theta}_y)$ and the function

$$\overline{I}_{\rm SR} = \int {\rm d}\alpha_i W_{if} \Phi_{\rm SR}(\alpha_i) \int {\rm d}\lambda W_\lambda |R(q_z)|^2, \tag{25}$$

determining the reflected flux integrated over angles θ_y, α_i and α_f with the resolution function $W_{if} = W_i(\overline{\alpha}_i - \alpha_i)W_f(\alpha_i - \overline{\alpha}_f)$, and the spectral function W_λ. Due to the $\delta-$function in Eq.(24) the integration over the azimuthal angles θ_y is removed and yields the factor $W_y(\overline{\theta}_y)$ describing the lineshape of the incident beam in the $y-$direction. Usually, SR is measured in the slit collimation relaxed in θ_y aiming to increase incident flux, while outgoing flux is integrated over the angle $\overline{\theta}_y$. As a result, the measured SR flux $\overline{I}_{\rm SR} = \overline{I}_{\rm SR}(\overline{\alpha}_i, \overline{\alpha}_f, \overline{\lambda})$ depends on three experimental variables, although the reflection coefficient $|R(q_z)|^2$ in Eq.(25) is a function of the single combination $q_z = (4\pi/\lambda)\sin\alpha_i$ of two theoretical variables λ and α_i.

The double integration in Eq.(25) has to be calculated numerically for each experimental point in 3D space with coordinates $\overline{\alpha}_i$, $\overline{\alpha}_f$ and $\overline{\lambda}$ inserting the model function for $|R(q_z)|^2$ and distribution functions W_i, W_f and W_λ computed for particular instrument parameters depending on the mode of operation. Then the result can be plotted

in the form of 2D flux distribution maps: $\overline{I}_{\rm SR}(\overline{\alpha}_i, \overline{\alpha}_f)$ at a fixed wavelength $\overline{\lambda}$, or $\overline{I}_{\rm SR}(\overline{\alpha}_f, \overline{\lambda})$ at a fixed incident angle $\overline{\alpha}_i$.

In the first case the SR distribution over the plane with Cartesian coordinate axes $\overline{\alpha}_i$ and $\overline{\alpha}_f$ is represented as a ridge running along the main diagonal $\overline{\alpha}_f = \overline{\alpha}_i$ of the map, while the width of the ridge is determined by the widths δ_f and δ_i. In the second case the SR ridge plotted in the map with coordinate axes $\overline{\alpha}_f$ and λ is running parallel to the coordinate λ at fixed position $\overline{\alpha}_f = \overline{\alpha}_i$ and the width dependents also on the wavelength.

In fact, the maps represent different cuts of the intensity distribution over the 3D space by that or the other 2D hyper-plane. However, in the case of SR any of these maps contains the same information about the 1D SLD profile encoded in the q_z dependence of $|R(q_z)|^2$. This information is usually extracted via fitting of the function $\overline{I}_{\rm SR}(q_z)$ in Eq.(25) additionally integrated over the outgoing angles $\overline{\alpha}_f$. Such integration results in the 1D function $\tilde{I}_{\rm SR}(\overline{q}_z)$ of the nominal wave vector transfer $\overline{q}_z$.

The general description above can be illustrated by the simple example when the functions $W_{i(f)}$ are approximated by the Gaussian functions,

$$W_{i(f)} = \frac{\exp\left[-(\overline{\alpha}_{i(f)} - \alpha_{i(f)})^2/(2\delta_{i(f)})^2\right]}{\sqrt{2\pi}\delta_{i(f)}}, \tag{26}$$

characterized by two parameters (Dorner & Wildes, 2003): the expectation value $\overline{\alpha}_{i(f)}$ and the dispersion $\delta_{i(f)}$. This substantially simplifies numerical calculations without a significant loss in accuracy.

Indeed, substitution of Eq.(26), into Eq.(25) yields the equation,

$$\overline{I}_{\rm SR}(\overline{\alpha}_i, \overline{\alpha}_f, \overline{\lambda}) = \frac{e^{-(\overline{\alpha}_i - \overline{\alpha}_f)^2/(2\delta^2)}}{2\sqrt{\pi}\delta} \tilde{I}_{\rm SR}(\overline{\alpha}, \overline{\lambda}), \tag{27}$$

which takes the form of a product of two functions. The first is simply the Gaussian of the difference $(\overline{\alpha}_i - \overline{\alpha}_f)$ with the mean square dispersion $\delta = \sqrt{\delta_i^2 + \delta_f^2}$ determining the width of the SR ridge. The second one depends on the weighted sum $\overline{\alpha} = (\overline{\alpha}_i \delta_f^2 +$

$\overline{\alpha}_f\delta_i^2)/\delta^2$ of incident and outgoing nominal angles and is represented as the integral,

$$\tilde{I}_{\rm SR}(\overline{\alpha},\overline{\lambda}) = \int {\rm d}\alpha \frac{e^{-(\overline{\alpha}-\alpha)^2/(2\overline{\delta}^2)}}{2\sqrt{\pi}\overline{\delta}} \Phi_{\rm SR}(\alpha)\overline{|R(\alpha,\overline{\lambda})|^2}^{\lambda}, \tag{28}$$

of the product of the Gauss function with the dispersion $\overline{\delta} = (\delta_i^{-2} + \delta_f^{-2})^{-1/2}$ and the reflection coefficient $|R(q_z)|^2$, where $q_z = (4\pi/\lambda)\sin\alpha$, averaged over wavelengths. This integral, as well as averaging over λ, determines the intensity variation along the SR ridge. In particular it smears out interference features of the reflection coefficient $|R(q_z)|^2$ suppressing high frequency interference fringes arising due to reflection from interfaces separated by distances greater than the transverse coherence length $l_z \sim \lambda/\overline{\delta}$. This length in our ToF experiments varies within the range 0.1 - 5 μm.

In contrast, the coherence length along the $x-$ axis at shallow incidence is typically extended up to the sub-millimeter range. Indeed, the coherence length $l_x \sim 1/\delta_x$ is determined by the uncertainty δ_x in wave vector transfer components q_x. This uncertainty is, in accordance with Eq.(1), mostly related to the width δ of the first Gaussian factor in Eq.(27), so that $\delta_x \approx q_z\delta/2$. Correspondingly, the coherence length $l_x \sim 2l_z/\delta \gg l_z$.

Note, that the angular divergence of the incident beam over angles θ_y determined by the width δ_y of the function $W_y(\theta_y)$ is usually much higher than $\delta_i \sim \delta_f \sim \delta$, so that $\delta_y \gg \overline{\delta} \gg \delta$. Therefore, the coherence length $l_y \sim 1/\delta_y \ll l_z \ll l_x$ is small and does not exceed 150 nm. This means that the coherence volume, often approximated by the ellipsoid reciprocal to the resolution ellipsoid, is extremely anisotropic with its longest principle axis colinear with the $x-$axis.

Moreover, each coherence ellipsoid covers only a very small percentage of the film volume. As a result experimentally measured reflectivity is actually an incoherent sum of SR from different coherent areas. Such incoherent averaging is trivial for laterally homogeneous films, while it may play an important role when this is not the case (Gorkov *et al.*, 2020) and the reflection potential varies within the film plane. Then

the consideration above is only valid for reflection potentials $\overline{U}(z) = \langle U(\boldsymbol{r}_{\|}, z)\rangle$ laterally averaged over the coherence area assuming that the result of such averaging is the same for all coherence ellipsoids. This may occur when the lateral dimensions of inhomogeneities, e.g. due to the SLD fluctuations, interface roughness, etc., are smaller than the coherence length l_x, so that each of the individual ellipsoids crosses a number of inhomogeneities. In this case, deviations $\Delta U(\boldsymbol{r}_{\|}, z) = U(\boldsymbol{r}_{\|}, z) - \overline{U}(z)$ of scattering potential from its mean value generate OSS considered in the next subsection. Alternatively, for inhomogeneities on a scale larger than l_x the averaging of the different reflection potentials has to be carried out incoherently, i.e. summing up of the (area weighted) reflectivities of each potential rather than averaging the potentials themselves. In the following we assume that inhomogeneities are much smaller than l_x but still larger than l_y.

2.8. Off-specular scattering amplitude and cross section

After the algorithm for computing the reference wave functions is settled for the mean SLD profile $\rho(z) = \langle\rho(\boldsymbol{r}^{\|}, z)\rangle$, averaged over all lateral inhomogeneities, one can calculate the differential cross section

$$\left(\frac{d\sigma}{d\Omega}\right)_{\text{OS}} = |f(\boldsymbol{k}_f, \boldsymbol{k}_i)|^2 \tag{29}$$

of OSS from deviations $\Delta\rho(\boldsymbol{r}) = \rho(\boldsymbol{r}) - \rho(z)$ of the SLD. The cross section in this equation, in contrast to Eq.(23) for SR, is determined by the OSS amplitude's modulus squared. The scattering amplitude is, by definition, an amplitude of spherical waves diverging from the source of scattering and hence, in contrast to the SR amplitude R, has the dimension of length. In the first order of the DWBA it is defined as a matrix element:

$$f(\boldsymbol{k}_f, \boldsymbol{k}_i) = -\int \mathrm{d}\boldsymbol{r}\Psi_f(-\boldsymbol{k}_f, \boldsymbol{r})\Delta\rho(\boldsymbol{r})\Psi_i(\boldsymbol{k}_i, \boldsymbol{r}), \tag{30}$$

of transition between initial and final neutron states distorted by the mean optical potential.

These states are described by wave functions factorized, as in Eq.(5) above, into products:

$$\Psi_i(\boldsymbol{k}_i, \boldsymbol{r}) = e^{i\boldsymbol{k}^i_\parallel \boldsymbol{r}_\parallel}\psi_i(z) \ \& \ \Psi_f(-\boldsymbol{k}_f, \boldsymbol{r}) = e^{-i\boldsymbol{k}^f_\parallel \boldsymbol{r}_\parallel}\psi_f(z), \tag{31}$$

of plane waves freely propagating parallel to the surface with the wave vectors $\boldsymbol{k}^i_\parallel$ and $-\boldsymbol{k}^f_\parallel$, while neutron propagation in the orthogonal direction above the surface is described by the transverse wave functions $\psi_i(z) = \psi(z, p_i)$ and $\psi_f(z) = \psi(z, p_f)$, where $p_i = k \sin \alpha_i$ and $p_f = k \sin \alpha_f$.

Here it is worth noting that the wave function $\Psi_f(-\boldsymbol{k}_f)$ in Eq.(30) corresponds to the wave propagating in the direction opposite to the scattered wave, and has little to do with the "time reversed" state (Sinha *et al.*, 1988; Durniak *et al.*, 2015). The latter would require complex conjugation, but not just changing a sign in front of the wave vector $\boldsymbol{k}_f$ pointing into the direction from the sample to the detector. The difference between time and space reversal becomes obvious below the critical edge of total reflection where the transverse component of the wave vector becomes totally imaginary. Then complex conjugation does not affect decaying exponents, while "space inversion" does.

The OSS cross section in Eq.(29) has a dimension of area and in principle can be directly compared with SR in Eq.(23). The latter is, however, defined only at $\alpha_f = \alpha_i$ and $\theta_y = 0$, turning to zero otherwise, while the former is a continuous function of α_f, α_i and θ_y. This is actually not a problem if one recognises that the quantities to be compared are simultaneously measured cross sections convoluted with the same resolution function.

In particular, the measured probability of SR $I_{\rm SR}$ in Eq.(25) should be compared with the corresponding dimensionless mean value, $I_{\rm OS} = I_{\rm OS}(\overline{\alpha_i}, \overline{\alpha_f}, \overline{\theta}_y, \overline{\lambda})$, defined as

the integral,

$$I_{\rm OS} = \int {\rm d}\alpha_i W_i(\overline{\alpha}_i - \alpha_i) \int {\rm d}\alpha_f W_f(\overline{\alpha}_f - \alpha_f)\Phi_{\rm OS}(\alpha_i) J_{\rm OS}, \tag{32}$$

where $\Phi_{\rm OS}$ is the illumination factor for OSS and the mean value $\overline{I}^{y,\lambda}_{\rm OS} = \overline{I}^{y,\lambda}_{\rm OS}(\alpha_f, \alpha_i)$.

The last term in eq. 32 is defined via the OSS cross section:

$$J_{\rm OS} = \int {\rm d}\theta_y W_y(\overline{\theta}_y - \theta_y) \int {\rm d}\lambda W_\lambda(\overline{\lambda} - \lambda) \frac{1}{S_{\rm OS}} \left(\frac{d\sigma}{d\Omega}\right)_{\rm OS}, \tag{33}$$

averaged over the azimuthal angle θ_y and the wavelength spread, and normalized to the sample area $S_{\rm OS} = S_{\rm OS}(\alpha_i)$ illuminated by the incident beam.

Such normalization is due to the fact that the OSS cross section is proportional to the area $S_{\rm OS}$ and results in the OSS illumination factor, $\Phi_{\rm OS}(\alpha_i) = S_{\rm OS}(\alpha_i)/S_b$ in Eq.(32). This factor is, in contrast to the similar factor $\Phi_{\rm SR}$ introduced above in Eq.(24), constant $\Phi_{\rm OS} = S_0/S_b = 1/\alpha_0 \gg 1$ at low angles of incidence $\alpha_i \leq \alpha_0$. Due to this factor, OSS is dramatically enhanced with respect to that of SR in the over-illumination regime often employed in monochromatic NR. If alternatively, the sample surface S_0 within the range $\alpha_i > \alpha_0$ becomes under-illuminated (which is usually the case in ToF NR) then the enhancement factor becomes $\Phi_{\rm SR} = 1/\alpha_i$, while still remaining quite large, but is reduced proportionally to the ratio $\alpha_0/\alpha_i \leq 1$. This reduction occurs just because a part of the sample at $\alpha_i > \alpha_0$ becomes shadowed by entrance slits and hence does not scatter neutrons.

Here we recall that the OSS cross section within the DWBA generally depends on four independent variables α_i, α_f, θ_y and λ, or four combinations of these variables: q_x from Eq.(1), q_y from Eq.(2),

$$p_i = \frac{2\pi}{\lambda} \sin\alpha_i \quad \text{and} \quad p_f = \frac{2\pi}{\lambda} \sin\alpha_f. \tag{34}$$

However, when presenting OSS data usually only three parameters q_z given in Eq.(3), q_x and q_y are used. All four running parameters are, in principle, accessible in the

2D 'pin-hole' collimation employed in experiments on Grazing Incidence Small Angle Scattering (GISANS) (Lauter *et al.*, 2016; Durniak *et al.*, 2015; Hexemer & Müller-Buschbaum, 2015; Theis-Bröhl *et al.*, 2008; Theis-Bröhl *et al.*, 2011). In this case two dramatically different lateral scales are probed simultaneously: the large one in q_x and the smaller one in q_y direction, but on the cost of reduced incident flux due to the fine in-plane collimation.

We will not go deeper into discussions on the GISANS cross-section, but in the following we will describe the OSS flux $\overline{I}_{\rm OS} = \overline{I}_{\rm OS}(\overline{\alpha}_i, \overline{\alpha}_f, \overline{\lambda}_i)$ integrated over angles θ_y as it is measured in the case of slit collimation. Hence the flux will depend on only three variables, and not on four, as $I_{\rm OS}$, while being still described by the same Eq.(32) in which the auxiliary function $J_{\rm OS}$ is substituted by the following integral:

$$\overline{J}_{\rm OS} = \int {\rm d}\lambda W_\lambda(\overline{\lambda} - \lambda) \frac{1}{S_{\rm OS}} \overline{\left(\frac{d\sigma}{d\Omega}\right)}^{y}_{\rm OS}, \tag{35}$$

where the bar over the scattering cross section denotes integration over the angle θ_y. This integration assumes that the resolution in $y-$direction is relaxed, so that the coherence length $l_y \leq \xi$, while the integral of $W_y(\overline{\theta}_y - \theta_y)$ over $\overline{\theta}_y$ turns to unity. Note that this assumption is not necessarily valid if the resolution in $y-$direction cannot be sufficiently relaxed, which may be the case on modern synchrotron X-ray reflectometers, or if the detector acceptance angle is too small.
At the same time OSS can be well resolved in orthogonal direction, i.e. in angles α_f and α_i, given the lateral coherence length l_x is larger than the correlation length ξ of SLD fluctuations.

2.9. OSS transverse form-factor in the DWBA

The DWBA cross section of OSS from layered structures into the upper hemisphere, can be readily calculated by the use of transverse wave functions (see Eqs.(31)) determined by Eq.(20) in which transmission amplitudes, t_l, are substituted by $t_l^i = t_l(p_i)$,

or $t_l^f = t_l(p_f)$, while reflection amplitudes, $\widetilde{r}_l$, are changed for $\widetilde{r}_l^i = \widetilde{r}_l(p_i)$, or $\widetilde{r}_l^f = \widetilde{r}_l(p_f)$, respectively. The phases φ_l in Eq.(20) are substituted by phases $\varphi_l^i = p_l^i d_l$, or $\varphi_l^f = p_l^f d_l$, depending on the wave numbers:

$$p_l^i = (p_i^2 - p_{cl}^2)^{1/2} \text{ or } p_l^f = (p_f^2 - p_{cl}^2)^{1/2}, \tag{36}$$

with the incident wave number, $p_i = k \sin \alpha_i$, determined by the angle of incidence incidence α_i, and the scattered wave number, $p_f = k \sin \alpha_f$, determined by the angle of scattering $\alpha_f \neq \alpha_i$.

The wave functions in Eqs.(31) for the layered model can be calculated substituting the layer's SLDs by their mean values $\rho_l(z) \approx \overline{\rho}_l$ defined in Eq.(12), while SLD deviations $\Delta\rho(\boldsymbol{r})$ are approximated with the same accuracy by the Riemann sum:

$$\Delta\rho(\boldsymbol{r}_\parallel, z) \approx \sum_{l=1}^{N} \Delta\rho_l(\boldsymbol{r}_\parallel), \tag{37}$$

in which $\Delta\rho_l(\boldsymbol{r}_\parallel) = \overline{\rho}_l(\boldsymbol{r}_\parallel) - \langle\overline{\rho}_l\rangle$. The mean value $\overline{\rho}_l(\boldsymbol{r}_\parallel)$ averaged over the layer thickness is defined in Eq.(37) by the equation,

$$\overline{\rho}_l(\boldsymbol{r}_\parallel) = \frac{1}{d_l} \int_{z_{l-1}}^{z_l} \mathrm{d}z \rho(\boldsymbol{r}_\parallel, z), \tag{38}$$

similar to Eq.(12), while the lateral averaging denoted by angular brackets is customarily defined as:

$$\langle\overline{\rho}_l\rangle = \frac{1}{S_{\mathrm{OS}}} \int \mathrm{d}\boldsymbol{r}_\parallel \overline{\rho}_l(\boldsymbol{r}_\parallel). \tag{39}$$

Further substitution of these equations and Eqs.(31) into Eqs.(30) yields the general DWBA expression for the scattering amplitude,

$$f(\boldsymbol{q}_\parallel; p_f, p_i) = -\sum_{l=1}^{N} d_l \Delta\overline{\rho}_l(\boldsymbol{q}_\parallel) F_l^\perp(p_f, p_i), \tag{40}$$

as a sum of "partial" amplitudes $f_l(\boldsymbol{q}_\parallel; p_f, p_i)$ of scattering from inhomogeneities in each layer l. These amplitudes are products of three factors. The first one is the layer

thickness d_l determining the dimension of a length for the scattering amplitude, while the other two factors are dimensionless.

The second factor,

$$\Delta\overline{\rho}_l(\boldsymbol{q}_\parallel) = \int \mathrm{d}\boldsymbol{r}_\parallel e^{-i\boldsymbol{q}_\parallel \boldsymbol{r}_\parallel} \Delta\overline{\rho}_l(\boldsymbol{r}_\parallel), \tag{41}$$

is the 2D Fourier transform of SLD deviations $\Delta\overline{\rho}_l(\boldsymbol{r}_\parallel)$. This factor is a function of the in-plane projection $\boldsymbol{q}_\parallel$ of the wave vector transfer $\boldsymbol{q}$. Due to the definition of the lateral average in Eq.(39) $\Delta\overline{\rho}(0) = 0$ and hence the scattering amplitude $f(0; p_f, p_i) = 0$.

The third factor in definition Eq,(40),

$$F_l^\perp(p_f, p_i) = \left[(t_l^f t_l^i + \widetilde{r}_l^f \widetilde{r}_l^i)F_l + (t_l^f \widetilde{r}_l^i + \widetilde{r}_l^f t_l^i)\widetilde{F}\right], \tag{42}$$

is composed of four combinations of transmission and reflection amplitudes multiplied by oscillating Laue-type functions,

$$F_l = \frac{e^{i(\varphi_l^f + \varphi_l^i)} - 1}{i(\varphi_l^f + \varphi_l^i)} \quad \text{and} \quad \widetilde{F}_l = \frac{e^{i\varphi_l^f} - e^{i\varphi_l^i}}{i(\varphi_l^f - \varphi_l^i)}, \tag{43}$$

in which phases $\varphi_l^f = p_l^f d_l$ and $\varphi_l^i = p_l^i d_l$ are determined by wave numbers p_f and p_i in Eqs.(36) and the layer thickness d_l.

The factor $F_l^\perp$ in Eq.(42) takes into account optical distortions of incoming and scattered neutron waves in the mean layer potential before and after scattering on the SLD deviations $\Delta\overline{\rho}_l$. It contains four terms proportional to all products of incident and scattered wave amplitudes, either both transmitted, $t_l^f t_l^i$, through the front face of the layer l, or both reflected $\widetilde{r}_l^f \widetilde{r}_l^i$ from its back face, as well as cross products $t_l^f \widetilde{r}_l^i$ and $\widetilde{r}_l^f t_l^i$ of transmission and reflection amplitudes. The sum of the two first terms in Eq.(42) is multiplied by the oscillating function $F_l = F_l(p_l^i + p_l^f)$ which decays at high values of the sum $\varphi_l^i + \varphi_l^f$ of phases, while $F_l = 1$ at $\varphi_l^i + \varphi_l^f = 0$. Similarly, the function $\widetilde{F}_l = \widetilde{F}_l(p_l^i, p_l^f)$ decays at high values of the difference $\varphi_l^i - \varphi_l^f$, while $\widetilde{F}_l = 1$ at $\varphi_l^i = \varphi_l^f$.

Further substitution of the scattering amplitudes in Eq.(30) yields the expression for the DWBA OSS cross section in Eq.(29):

$$\left(\frac{d\sigma}{d\Omega}\right)_{\rm OS} = S_{\rm OS} \sum_{ll'} G^{\perp}_{ll'}(p_f, p_i) G^{\|}_{ll'}(\boldsymbol{q}_{\|}). \tag{44}$$

The OSS cross section is therefore proportional to the area $S_{\rm OS}$ of the sample illuminated by the neutron beam and to the weighted double sum of products of the dimensionless form-factors: the transverse, $G^{\perp}_{ll'}(p_f, p_i)$, and the lateral one, $G^{\|}_{ll'}(\boldsymbol{q}_{\|})$.

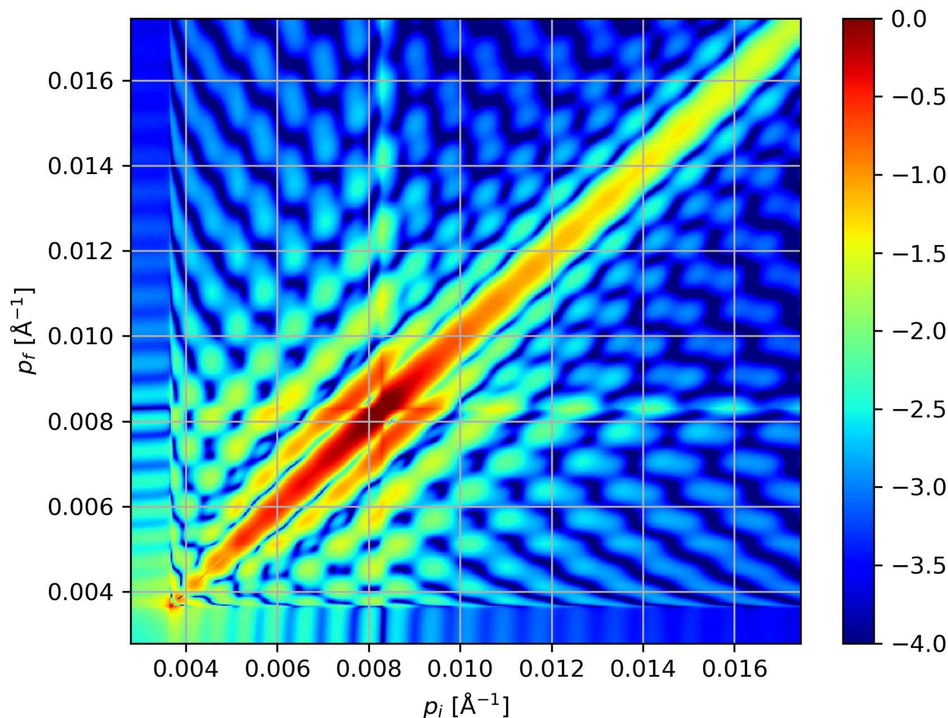

Fig. 4. The transverse form-factor calculated for the thick top layer of the same h-PMMA/d-PS bilayer on a silicon substrate as used to illustrate the wave field distribution in Fig. 3.

The partial transverse form-factor,

$$G^{\perp}_{ll'}(p_f, p_i) = F^{\perp}_{l}(p_f, p_i) F^{\perp *}_{l'}(p_i, p_f), \tag{45}$$

in Eq.(44) is expressed via products of the function F_l for the lth layer and the complex conjugate $F_{l'}^{\perp *}$ for the layer l'. These products, $G_{ll'}^{\perp} = G_{ll'}^{\perp}(p_f, p_i)$, in the sum in Eq.(44) are functions of two variables independent of each other being components p_i and p_f of incoming and outgoing wave vectors $\boldsymbol{k}_i$ and $\boldsymbol{k}_f$.

The transverse form-factor's dependence on p_i and p_f can be visualized in a 2D map shown in Fig. 4. The map, resembling a Chladni nodal pattern, is calculated for the contribution $G_{11}^{\perp}(p_f, p_i)$ of the top thick layer for the same model as has been used for Fig. 3. The map exhibits a detailed pattern demonstrating an integral effect of sixteen terms contributing to the single ingredient $G_{11}^{\perp}(p_f, p_i)$ of the sum in Eq.(44). An example of the analysis of different contributions is presented in the Supporting Information (SI). Here we only mention that OSS is substantially enhanced within the ranges $p_{c2} \leq p_i \leq p_{c1}$ and/or $p_{c2} \leq p_f \leq p_{c1}$. The amplitudes of incident and/or scattered waves in Fig. 3 acquire an appreciable interference enhancement, which becomes most significant at $p_i \approx p_f$, i.e. along the ridge running the main diagonal, where the SR would be situated (excluded from the map).

All features in Fig. 4 are solely due to the reference layered structure, the parameters of which are determined from the fit of SR. Therefore, at first sight, it does not provide any extra information about in-plane inhomogeneities. This, however, is not not completely true and, as is illustrated in the Supporting Information, an analysis of different features in the maps of transverse form-factors is quite important in determining the depth location of lateral inhomogeneities causing OSS and therefore excluding or corroborating the model used for the SR fitting, similar to an additional scattering contrast in SR.

2.10. OSS lateral form-factor in the DWBA

The new information inaccessible by SR is encoded in the lateral form-factor:

$$G^{\|}_{ll'}(\boldsymbol{q}_{\|}) = d_l d_{l'} \int \mathrm{d}\boldsymbol{r}_{\|} e^{-i\boldsymbol{q}_{\|}\boldsymbol{r}_{\|}} g_{ll'}(\boldsymbol{r}_{\|}). \tag{46}$$

It is proportional to the *correlator* which is the 2D Fourier transform of the in-plane *pair correlation function* of SLD deviations. This function can be generally defined as a 2D integral:

$$g_{ll'}(\boldsymbol{r}_{\|}) = \frac{1}{S_{\mathrm{OS}}} \int \mathrm{d}\boldsymbol{r}'_{\|} \Delta\overline{\rho}_l(\boldsymbol{r}_{\|} + \boldsymbol{r}'_{\|}) \Delta\overline{\rho}^{*}_{l'}(\boldsymbol{r}'_{\|}), \tag{47}$$

running over the sample surface area S_{OS} illuminated by the neutron beam. The integrand here is a product of the SLD deviations and its image shifted by the in-plane radius-vector $\boldsymbol{r}_{\|}$. Hence the integrand in Eq.(47) is proportional to the area of their overlap, as is illustrated in Fig.5 for an example of the layer containing inclusions of foreign material in the form of cylinders, or discs, with height equal to the layer thickness d_l and randomly distributed over the layer plane.

The overlap area is proportional to the number of inclusions and hence the sample surface area illuminated by the incident beam. Therefore the normalization constant S_{OS} in Eq.(47) is cancelled out and the correlation function $g_{ll'}(\boldsymbol{r}_{\|})$ is independent of S_{OS}. Strictly speaking, the definition of the correlation function $g_{ll'}(\boldsymbol{r}_{\|}) = \langle \Delta\overline{\rho}_l(\boldsymbol{r}_{\|}) \Delta\overline{\rho}^{*}_{l'}(0) \rangle$ in Eq.(47) holds for statistically homogeneous matter under the hypothesis of self-averaging in the "thermodynamic limit" $S_{\mathrm{OS}} \to \infty$. In this limit a contribution of surface boundaries into the integrals in Eq.(47) and Eq.(46) can be neglected. This is, actually, well justified if the *correlation length* ξ determining a distance $|\boldsymbol{r}_{\|}| \leq \xi$ at which correlations are significant, is much smaller than the surface linear dimensions.

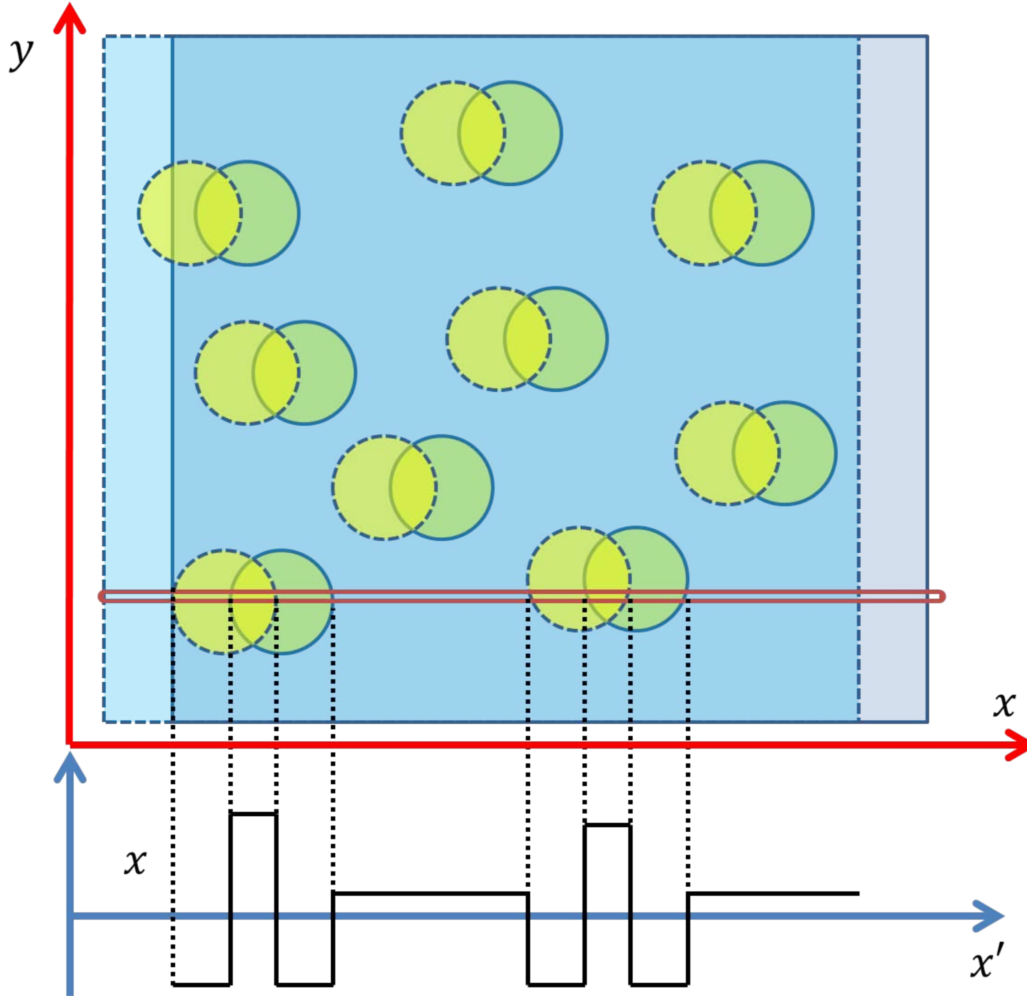

Fig. 5. Illustration of the integrand in Eq.(47): the product of SLD deviations $\Delta\overline{\rho}^*_{l'}(\boldsymbol{r}'_{\|})$ and its conjugated image shifted by a distance $r_{\|}$ along the x-axis, $\Delta\overline{\rho}_l(\boldsymbol{r}_{\|}+\boldsymbol{r}'_{\|})$. Below: The image profile along the line $y = y' = const$.

In general, parameters determining the in-layer correlation function may vary from layer to layer and, in particular, the correlation length $\xi = \xi_l$ may depend on the layer number l, while SLD deviations may be correlated in neighboring layers, or through the whole multilayer stack. This can be taken into account for arbitrary in-plane and depth-dependent distributions of SLD deviations via choosing a suitable set of layers in Eq.(44) in accordance with the assumed model for the depth-dependent correlation

function $g_{ll'}(\boldsymbol{r}_{\|})$. In particular, if deviations in different layers are not correlated then the correlation function $g_{ll'}(\boldsymbol{r}_{\|}) = g_{ll}(\boldsymbol{r})_{\|}\delta_{ll'}$ and the sum in Eq.(44) contains only diagonal elements with $l = l'$. If, alternatively, deviations are correlated over a certain number of layers with an out-of-plane correlation length ν exponentially decaying when $|l - l'| > \nu$ then instead of the Kronecker symbol $\delta_{ll'}$ one may introduce the factor $\exp(-|l - l'|/\nu)$. Setting the depth-dependent correlation parameter $\nu \gg N$ results in correlations extended over all layers. The choice of the particular depth-dependent correlation function and its consequences may be of a particular importance for heterostructures with large number of layers, detailed consideration of which is far beyond the scope of this work.

Instead, let us briefly analyse the general behavior of the lateral correlation function and correlator in the single layer l. First of all, one may expect that at $|\boldsymbol{r}_{\|}| \ll \xi_l$ the correlation function $g_{ll}(0) = \langle|\overline{\rho}_l|^2\rangle - |\langle\overline{\rho}_l\rangle|^2$ is almost independent of coordinate r and proportional to ξ_l^2, while in the opposite limit of large distances, $|\boldsymbol{r}_{\|}| \gg \xi_l$, correlations vanish. This is an immediate consequence of the hypothesis on correlations decoupling when $|\boldsymbol{r}_{\|}| \to \infty$: in this limit $g_{ll}(\boldsymbol{r}_{\|}) \approx \langle\Delta\overline{\rho}_l(\boldsymbol{r}_{\|})\rangle\langle\Delta\overline{\rho}_l^*(0)\rangle \to 0$ and the integral in Eq.(47) tends to zero. Let us also assume that the correlation function decays exponentially, or faster, so that the integral in Eq.(46) converges. Moreover, let us suppose that the function $g_{ll}(\boldsymbol{r}_{\|})$ is characterized by the single parameter ξ_l. Then, in the limit of low $q_{\|} \le \xi_l^{-1}$ the correlator in Eq.(46) $G_{ll}^{\|}(\boldsymbol{q}_{\|}) \sim \xi_l^2$ (except for the case $q = 0$, where it should turn to zero). Correspondingly, the OSS cross section in Eq.(44) can be estimated at low q_x and $G_{ll}^{\perp} \sim 1$ as a product $S_{\mathrm{OS}} d_l^2 \xi_l^2 |\Delta\overline{\rho}_l|^2$. The latter for sufficiently thick layers and extended in-plane correlation length may become quite large and even exceed the illuminated sample area S_{OS}. If this happens one may suspect that the BA, as well as the DWBA, fail. This is, however, not the case if all OSS (or GISANS) is concentrated within a sufficiently small window of scattering

angles $\alpha_f \ll 1$ and $\theta_y \ll 1$. As a result the total scattering cross section may still be much smaller than $S_{\rm OS}$ and the DWBA may be still valid.

A particular asymptotic behavior of the integral in Eq.(46) at $q_x \gg \xi_l^{-1}$ generally depends on the decay rate of the correlation function $g_{ll}(r_\parallel)$ in direct space, as well as on global symmetry of the film and the dimension of the Fourier transform. If, for instance, the function $g_{ll}(r_\parallel)$ decays exponentially, or faster (but slower than the Gauss function) and independent of the direction of the in-plane radius-vector $\boldsymbol{r}_\parallel$ then $G_{ll}(q_\parallel)$ decays as $q_\parallel^{-3}$ for a 2D Fourier transform.

This can be illustrated by the simple example of the model correlation function $g_{ll}(\boldsymbol{r}_\parallel) = \langle|\Delta\bar{\rho}_l|^2\rangle \exp(-|\boldsymbol{r}_\parallel|/\xi_l)$ matching short and long range correlations via the 'soft exponential cut-off' of the latter. As we shall see later, this simple function is able to describe our experimental data introducing a single parameter ξ_l. This is possible despite of the fact that the overlap area in Eq.(47) for a single circle in Fig. 5 experiences a rather 'hard cut off' when the distance between a circle and its shifted image is equal to the circle diameter. As a consequence, the Fourier transform in Eq.(46) is expressed via a Bessel function revealing periodic fringes and superimposed with a $q_\parallel^{-3}$ decay. However, such fringes are washed out after averaging over a broad distribution of shapes and sizes of cylinders, as well as over their positions (see Supporting Information (SI) for details).

The 2D Fourier transform in Eq.(46) of the exponential correlation function has the following explicit form:

$$G_{ll}^{\parallel}(\boldsymbol{q}_\parallel) = 2\pi\langle|\Delta\bar{\rho}_l|^2\rangle d_l^2\xi_l^2[1 + (q_\parallel\xi_l)^2]^{-3/2}, \qquad (48)$$

providing smooth interpolation between low and high $q_\parallel$ asymptotic behavior. With the correlator in Eq.(48) the OSS cross section in Eq.(44) becomes in the low q limit ($q_\parallel\xi_l \ll 1$, $p_i d_l \ll 1$ and $p_f d_l \ll 1$) proportional to the dimensionless factor $2\pi d_l^2\xi_l^2\langle|\Delta\bar{\rho}_l(0)|^2\rangle$ multiplied by the illuminated sample surface $S_{\rm OS}$.

The asymptotic decay of the function in Eq.(48) as $q_{\|}^{-3}$ is in a full accord with the Porod law decay rate q^{-4} which is appropriate for a conventional SANS measured from 3D systems at normal incidence onto the sample surface. Then at $q \gg \xi_l^{-1}$ the Born Approximation (BA) usually applies (Maleev & Toperverg, 1980) and the scattering amplitude is proportional to the 3D (but not 2D, as in Eq.(46)) Fourier transform of the spherically symmetric mean scattering potential. The extra dimension of the Fourier integral increases the asymptotic decay power of the scattering cross section in the BA from -3 to -4. In particular, for an exponential decay of the correlation function the SANS cross section is proportional to the sample area S illuminated by the incident beam and the dimensionless factor $8\pi\langle|\Delta\rho|^2\rangle d\xi^3[1+(q\xi)^2]^{-2}$ (Cowley, 1987; Runov *et al.*, 1991). Here d denotes the sample thickness, while the squared Lorentzian, decays as q^{-4} when $q \gg \xi^{-1}$.

Note that the coherence area in SANS experiments with pin-hole collimation is nearly isotropic in the $x-y$ surface plane parallel to the detector plane. Usually both in-plane coherence lengths $l_x \sim l_y$ may amount up to only a few hundreds of nanometers, while the longitudinal coherence length $l_z \gg l_x \sim l_y$ in the direction along the beam and normal to the surface may be extended up to dozens of micrometers. This is apparently due to the fact that in SANS the longitudinal component q_z of the wave vector transfer is extremely small. Actually, it is usually neglected so that the absolute value of the wave vector transfer approximates to $q \approx (q_x^2+q_y^2)^{1/2}$. In contrast, the longitudinal component of the wave vector transfer q_x in GISANS cannot generally be neglected, although it is much smaller than two other components q_z and q_y. Indeed, in accordance with Fig.1, this component at grazing incidence and scattering is almost parallel to the $x-$axis within the surface plane and equal to q_x, but not q_z as in the case of SANS. Therefore, as discussed above, the uncertainty δq_x is much smaller than uncertainties δq_y and δq_z resulting in strong anisotropy of the coherence area within

the surface plane, so that $l_x \gg l_y \sim l_z$.

Due to this anisotropy GISANS can, in principle, simultaneously probe two drastically different scales, or correlation lengths, in the surface plane: the same scale as in SANS up to 100 nm in the $y-$direction direction and the much larger one in the $x-$direction. If the lateral correlation length is unique and the on the scale accessible for SANS then the q_x component of the wave vector transfer in Eq.(48) can be safely neglected, and the lateral form-factor is approximated as: $G^{\|}_{ll}(\boldsymbol{q}_{\|}) \approx G^{\|}_{ll}(q_y)$.

At the same time, the GISANS cross section, in contrast to that of SANS, crucially depends on the q_z component normal to the surface via the transverse structure factor $G^{\perp}_{ll'}(p_f, p_i)$ in Eq.(45). The latter, as explained in the previous Subsection, is mostly determined by the mean SLD profile laterally averaged over the coherence area, i.e over l_x and l_y. Such specific averaging becomes especially tricky in the case of surfaces laterally decorated with a variety of 3D elements of low symmetry (Durniak *et al.*, 2015). In this case full recovery of 3D shapes from a single 2D $y - z$ (but not $x - y$) Fourier transform is hardly possible even in the BA, as it requires to jointly evaluate a set of GISANS images recorded along principle symmetry in-plane directions via rotating the sample around its normal. Moreover, the DWBA should be then formulated and applied for each of those directions taking into account an interplay between coherent and incoherent scattering due to high anisotropy of in-plane coherency. We shall not address here this challenging problem, but rather concentrate on the easier case of OSS from a statistically isotropic distribution of inhomogeneities over the surface plane.

First of all, one may note that, in contrast to SANS and GISANS, the OSS cross section requires one to calculate the 1D, but not 2D, lateral Fourier transform in Eq.(46). This is due to the fact that OSS is usually recorded simultaneously and with the same slit collimation conditions as SR, i.e. with the resolution relaxed along

$y-$direction and with the fine collimation in the $z-$direction. Correspondingly, the coherence length l_y is rather short along $y-$axis, while l_x is dramatically extended in the x direction, so that coherence ellipsoids degenerate into a set of long and thin bars, one of which is indicated in Fig. 5 by the double line running parallel to the $x-$axis and crossing certain number of lateral inhomogeneities. If the mean distance between inhomogeneities is much smaller than the coherence length, the OSS cross section is determined by the former lateral form-factors incoherently summed over different coherence ellipsoids covering the sample surface. Alternatively, interference between scattering from different inhomogeneities crossed by an ellipsoid allows to probe correlations between their positions. In particular, a periodic distribution of such inhomogeneities would result in Bragg scattering, for which the cross section is, however, measured as an incoherent sum of cross sections corresponding to different coherence ellipsoids.

Due to the strong anisotropy of coherence properties, the lateral correlator $G_{ll'}(q_x, q_y)$ in Eq.(46) determining the OSS probability in Eq.(35) can be safely substituted by its value $\overline{G}^y_{ll'}(q_x)$ integrated over scattering angles θ_y. Taking into account the fast decay of the integrand within the range of $\theta_y \ll 1$, integration can be readily accomplished over the projection $q_y \approx (2\pi/\lambda)\theta_y$ of the lateral wave vector transfer.

As a result, the 1D function $\overline{G}^y_{ll'}(q_x)$ is finally expressed via the Fourier transform:

$$\overline{G}^y_{ll'}(q_x) = \lambda \int \mathrm{d}x e^{-iq_x x}\, \overline{g}^y_{ll'}(x), \tag{49}$$

of the correlation function $\overline{g}^y_{ll'}(x) = g_{ll'}(x, 0)$ determined by the same Eq.(46), but with $y = 0$. From Eq.(49) it follows that for a function $g_{ll'}(x)$ decaying at least exponentially (but slower than a Gauss function for large distances) the correlator $\overline{G}^y_{ll'}(q_x)$ decays at $q_x\xi_l \gg 1$ as q_x^{-2}, i.e. much slower than 3D or 2D Fourier transforms of the correlation function. On the other hand, in the opposite limit $q_x\xi_l \ll 1$ it is proportional to the small factor $\lambda\xi_l$ instead of the factor ξ_l^2 in 2D case. This substantially reduces the OSS

cross section whose value is now estimated as $S_{\rm OS}\langle|\Delta\overline{\rho}_l|^2\rangle d_l^2\lambda\xi_l$.

As above, the low and high q_x asymptotics can be matched with straightforward calculation of the 1D Fourier transform in Eq.(49) for the case of the exponential form $\overline{g}^y_{ll}(x) = g_{ll}(0)\exp(-q_x\xi_l)$ of the correlation function. Then, instead of Eq.(48), the correlator,

$$\overline{G}^y_{ll}(q_x) = 2\langle|\Delta\overline{\rho}_l|^2\rangle d_l^2\lambda\xi_l[1 + (q_x\xi_l)^2]^{-1}, \quad (50)$$

is proportional to the Lorentz function. It reaches the maximum value at $q_x\xi_l \ll 1$. This value is a few orders of magnitude smaller than that in Eq.(48) for GISANS. Therefore, at first sight, one may suppose that measurements of the GISANS are less time-consuming than OSS.

This conclusion is, however, not fairly correct. First of all one should admit that pin-hole collimation significantly reduces neutron flux incident onto the sample surface. Moreover, at sufficiently large $\xi_l \sim q_x^{-1}$, ranging between 100 nm and 0.1 mm, the GISANS signal is usually not resolved in the q_y direction, as the scattering in the $y-$direction is almost entirely concentrated within the width δ_y of the resolution function $W_y(\theta_y)$ in Eq.(32) centered at the position $\overline{\theta}_y = 0$. This can be readily confirmed via a direct convolution of the correlator in Eq.(48) with the resolution function providing the same result as Eq.(50).

Hence, pin-hole collimation does not manifest any benefit for large in-plane correlations and just leads to substantial losses in luminosity. Therefore, GISANS is applied to probe relatively small correlation lengths, $\xi_l \leq \lambda/\delta_y$, ranging up to $\sim$ 100 nm, commensurate with the inverse uncertainty in the wave vector transfer component q_y. In this constraint the absolute maximum of the scattering signal is proportional to ξ_l^2, but by several orders of magnitude smaller than at the large ξ_l probed by OSS.

The general consideration above is further illustrated in the SI with an example based on the Cowley-Krivoglaz (Cowley, 1950; Krivoglaz, 1969) theory for diffuse

scattering from decaying binary alloys. Their results can be generalized for the case when one, or some number of bilayers comprise two immiscible sub-phases leading to lateral domains consisting of one of species embedded into the matrix of the other. Such decomposition may suddenly occur at a certain temperature sufficient to overcome the potential barrier between laterally homogeneous and inhomogeneous states. Alternatively an increase of the statistical interface roughness, e.g. between immiscible polymer layers in contact through a common interface, may preclude the decomposition of the layers. In this case it is usually assumed that the ideally flat interface is perturbed by long wavelength thermal excitations with a continuous spectrum. Such excitations propagating along the interface in the form of low amplitude waves, e.g. capillary, are customarily described within the framework of linear hydrodynamics introducing a cut-off parameter maintaining a small wave amplitude.

This is particularly necessary in the case of capillary waves the amplitude of which formally diverges logarithmically in the infrared limit. There are several physical reasons for cutting-off wave amplitudes: interaction with a solid flat substrate, gravity, bending rigidity, finite size effects, etc. However, one may expect that the ideally flat infinite common interface between layers of immiscible polymers is not a real ground state of the system. In particular, it may be unstable with respect to highly nonlinear types of excitations violating lateral continuity of one or both layers via formation of e.g. microscopic pores reducing the area of unfavorable interfacial contact, if their lateral dimensions are smaller than the layer thickness. Such pores may be partially, or totally filled with the neighboring layer material, forming flat cylinder-like protuberances entering into, or running though a sufficiently thin layer.

2.11. OSS from interface roughness in the DWBA

The general procedure of the DWBA described in the Subsection 2.8 can be readily applied to the case of statistical interfacial roughness perturbing the reference interaction potential. The latter has been chosen in the Subsection 2.5 as averaged over interface position fluctuations hence proving smooth variation of SLD between its values ρ_{l-1} and ρ_l in neighboring layers. Such variation is often approximated by the error function in Eq.(22) providing a description of SR from rough interfaces in e.g. a high q limit. In principle, it can be also used to modify (Tolan, 1998), if necessary, reference wave functions in Eq.(30) for the amplitude of OSS caused by roughness-induced SLD deviations $\Delta\rho_l(\boldsymbol{r}_\parallel, z)$ of SLDs from their mean values $\overline{\rho}_l(z) = \langle\rho(\boldsymbol{r}_\parallel, z)\rangle$. Then the use of accordingly modified wave functions in the definition in Eq.(30) may reasonably describe OSS in a broad range of wave vector transfers and also guarantee that the DWBA OSS amplitude and cross section become zero at $q = 0$.

On the other hand, at $q \neq 0$ one can conveniently redefine Eq.(30) in such a way (Sinha *et al.*, 1988), that each term of the sum,

$$f(\boldsymbol{q}_\parallel; p_f, p_i) = -\sum_{l=1}^{N+1} \Delta\tilde{\rho}_l \int \mathrm{d}\boldsymbol{r}_\parallel e^{-i\boldsymbol{q}\boldsymbol{r}_\parallel} \mathcal{F}_l(\boldsymbol{r}_\parallel), \tag{51}$$

running over all interfaces, is proportional to the SLD contrast $\Delta\tilde{\rho}_l = (\rho_{l-1} - \rho_l)$ between SLD in the bulk of neighboring layers comprising the $(l-1)$ rough interface.

The function $\mathcal{F}_l(\boldsymbol{r}_\parallel) = \mathcal{F}_l(\boldsymbol{r}_\parallel; p_i, p_f)$ in Eq.(51),

$$\mathcal{F}_l(\boldsymbol{r}_\parallel) = \int_{\overline{z}_{l-1}}^{z_{l-1}^{>}} \mathrm{d}z \psi_l^f(z)\psi_l^i(z) - \int_{z_{l-1}^{<}}^{\overline{z}_{l-1}} \mathrm{d}z \psi_{l-1}^f(z)\psi_{l-1}^i(z), \tag{52}$$

is determined via the difference between two 1D integrals which, however, do not coexist at the same lateral coordinate $\boldsymbol{r}_\parallel$. The first of them is running over the z coordinate from the mean interface at $\overline{z}_{l-1}$ up to the actual surface coordinate $z_{l-1}^{>} = \overline{z}_{l-1} + h_{l-1}^{>}$ which at a given in-plane coordinate $\boldsymbol{r}_\parallel$ deviates from the mean interface

position by a distance $h^{>}_{l-1} = h^{>}_{l-1}(\boldsymbol{r}_{\parallel}) > 0$. Within this range of $\boldsymbol{r}_{\parallel}$ the second integral is zero, wile alternatively, it runs over the interval from $z_{l-1} - h^{<}_{l-1}(\boldsymbol{r}_{\parallel})$ up to $\overline{z}_{l-1}$ at the in-plane coordinates $\boldsymbol{r}_{\parallel}$ inside areas of the actual interface displayed below the mean interface. Within this range of the coordinate $\boldsymbol{r}_{\parallel}$ the first integral is equal to zero.

The integrands in Eq.(52) are equal to products of incoming, $\psi^{i}_{l}(z)$, and outgoing, $\psi^{f}_{l}(z)$, wave functions distorted in either the mean SLD of the layer l, or functions $\psi^{i}_{l-1}(z)$ $\psi^{f}_{l-1}(z)$ distorted in the mean SLD of the layer $l-1$, respectively. Regrettably, there is no solution known for the wave equation with the error function in Eq.(22) describing the mean SDL variation in the case of Gaussian roughness.

Therefore, the wave functions of a smooth interface,

$$\psi^{i,f}_{l}(z) = t^{i,f}_{l} e^{ip^{i,f}_{l}(z-z_{l-1})} + r^{i,f}_{l} e^{-ip^{i,f}_{l}(z-z_{l-1})} \tag{53}$$

calculated in accordance with Eq.(13), or Eq.(20) are often used instead of the exact ones (Sinha *et al.*, 1988). These solutions are valid in homogeneous depth-profiles and can still be used in the interface region where the SLD strongly varies as a function of depth. This assumption looks quite reasonable in the case of low roughness concentrated in the interface vicinity such that its contribution into the integral in Eq.(52) is small and can be either neglected, or phenomenologically taken into account via modification of transmission, $t^{i,f}_{l}$, and reflection,$r^{i,f}_{l}$, amplitudes by Nevot-Croce factors (Nevot & Croce, 1980).

The integration in Eq.(52) with wave functions from Eq.(53) can now be readily resulting in the following equation,

$$f(\boldsymbol{q}_{\parallel}; p_f, p_i) = -\sum_{l=1}^{N+1} \Delta\tilde{\rho}_l h_{l-1}(\boldsymbol{q}_{\parallel})(t^{i}_{l} + r^{i}_{l})(t^{f}_{l} + r^{f}_{l}), \tag{54}$$

describing the OSS amplitude of all possible transitions between waves propagating in bulk of neighboring layers above and below the interface $(l-1)$.

In this equation the function

$$h_{l-1}(\boldsymbol{q}_{\|}) = \int \mathrm{d}\boldsymbol{r}_{\|} e^{-i\boldsymbol{q}\boldsymbol{r}_{\|}} h_{l-1}(\boldsymbol{r}_{\|}), \tag{55}$$

is the in-plane 2D Fourier transform of the deviation $h_{l-1}(\boldsymbol{r}_{\|}) = h^{>}_{l-1}(\boldsymbol{r}_{\|}) - h^{<}_{l-1}(\boldsymbol{r}_{\|})$ which randomly varies as a function of the in-plane variable $\boldsymbol{r}_{\|}$ and changes sign whenever either $h^{>}_{l-1}(\boldsymbol{r}_{\|})$, or $h^{<}_{l-1}(\boldsymbol{r}_{\|})$ turn into zero. This happens when $h^{>}_{l-1}(\boldsymbol{r}_{\|}) = h^{<}_{l-1}(\boldsymbol{r}_{\|}) = 0$. Due to this equation the OSS amplitude at $f(0) = 0$ and does not contribute to SR.

Further substitution of Eq.(55) into Eq.(54) and Eq.(29) yields the expression,

$$\left(\frac{d\sigma}{d\Omega}\right)^{\mathrm{h}}_{\mathrm{OS}} = S_{\mathrm{OS}} \sum_{ll'} \mathcal{G}^{\perp}_{ll'}(p^f, p^i)\mathcal{G}^{\|}_{ll'}(\boldsymbol{q}_{\|}), \tag{56}$$

for the DWBA OSS cross section from rough interfaces.

This expression is similar to that in Eq.(44), in which the transverse form-factor $G^{\perp}(p^f_i, p^i)$ in Eq.(45) is substituted by the factor,

$$\mathcal{G}^{\perp}_{ll'}(p^f, p^i) = (t^f_l + r^f_l)(t^i_l + r^i_l)(t^f_{l'} + r^f_{l'})^*(t^i_{l'} + r^i_{l'})^*, \tag{57}$$

which does not contain oscillating functions F_l and $\widetilde{F}_l$ in Eq.(43). This means that for OSS arising from roughness only the oscillations of the neutron field coming from the layer thickness (at constant $p_i + p_f$ and $p_i - p_f$) are not present, hence providing an image depicted in Fig.6 smoother than that in Fig. 4 as only enhancements along constant $p_{i/f}$ values are present. Hence, this qualitative difference between Figs.4 and 6 allows one to distinguish between correlated roughness and bulk defects without any quantitative analysis when plotting the data in this space. This important tool will be further illustrated in secs. 3 and 4.

The correlator of SLD deviations $G^{\|}_{ll'}$ given in Eq.(46) is changed in Eq.(56) for the correlator,

$$\mathcal{G}^{\|}_{ll'}(\boldsymbol{q}_{\|}) = \Delta\tilde{\rho}_l \Delta\tilde{\rho}^*_{l'} \int \mathrm{d}\boldsymbol{r}_{\|} e^{-i\boldsymbol{q}_{\|}\boldsymbol{r}_{\|}} \tilde{g}_{ll'}(\boldsymbol{r}_{\|}), \tag{58}$$

expressed via the 2D Fourier transform of the height-height correlation function $\tilde{g}_{ll'}(\boldsymbol{r}_\parallel) = \langle h_{l-1}(\boldsymbol{r}_\parallel) h_{l'-1}(0)\rangle$.

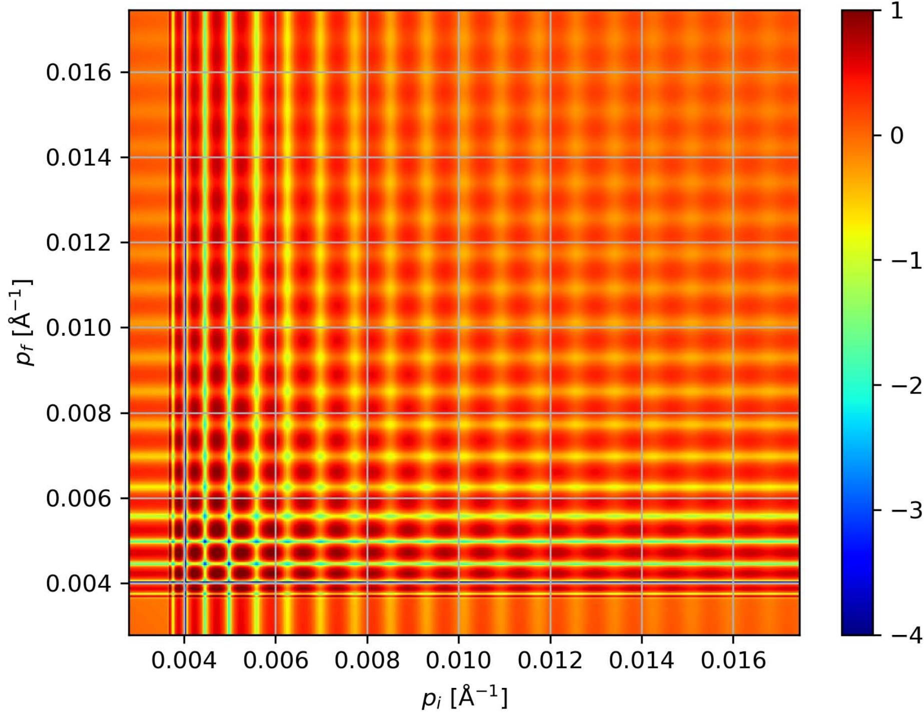

Fig. 6. Simulated pattern of the transverse correlator $\mathcal{G}^{\perp}_{ll'}(p^f, p^i)$ in Eq.(57) for $l = l' = 0$ and the same model parameters as used in Figs. 3 and 4.

The latter function is proportional to the 2D Fourier transform of the in-plane height-height correlation function $\tilde{g}_{ll'}(\boldsymbol{r}_\parallel) = \langle h_{l-1}(\boldsymbol{r}_\parallel) h_{l'-1}(0)\rangle$ and can be defined as the 2D integral:

$$\tilde{g}_{ll'}(\boldsymbol{r}_\parallel) = \frac{1}{S_{\mathrm{OS}}} \int \mathrm{d}\boldsymbol{r}'_\parallel h_{l-1}(\boldsymbol{r}_\parallel + \boldsymbol{r}'_\parallel) h_{l'-1}(\boldsymbol{r}'_\parallel). \tag{59}$$

If deviations are not correlated at different interfaces then $\tilde{g}_{ll'}(\boldsymbol{r}_\parallel) = \tilde{g}_{ll}(\boldsymbol{r}_\parallel)\delta_{ll'}$ and the integrand in Eq.(59) is a product of the deviation $h_{l-1}(\boldsymbol{r}_\parallel)$ and its image $h_{l-1}(\boldsymbol{r}'_\parallel + \boldsymbol{r}_\parallel)$ shifted along mean interface for the in-plane radius-vector $\boldsymbol{r}_\parallel$. Hence the integrand in Eq.(59) is proportional to the area of their overlap.

From Eq.(59) it is quite obvious that the correlation function $\tilde{g}_{ll}(0) = \sigma_{l-1}^2$ is equal to the r.m.s roughness squared $\sigma_{l-1}^2 = \langle h_{l-1}^2 \rangle$. One may also expect that at large distances $|\boldsymbol{r}_{\parallel}|$ much greater than the correlation length ξ_l, correlations become decoupled, so that the correlation function $\tilde{g}_{ll}(\boldsymbol{r}_{\parallel}) = \langle h_{l-1} \rangle \langle h_{l-1} \rangle \to 0$ vanishes.

Quite often, roughness of surfaces and interfaces reveal self-affinity and supposed to behave as a surface fractal (Mandelbrot *et al.*, 1984). In this case the decay of the correlation function can be described (Sinha *et al.*, 1988) by the fractional exponent:

$$\tilde{g}_{ll}(r) = \sigma_{l-1}^2 \exp\left[-\left(r_{\parallel}/\xi_{l-1} \right)^{2\mathcal{H}} \right] , \tag{60}$$

with $r_{\parallel} = |\boldsymbol{r}_{\parallel}|$ and the Hurst parameter $\mathcal{H}$.

Substituting Eq.(60) into Eq.(58) one can readily obtain an explicit expression for the correlator $\mathcal{G}_{ll}^{\parallel}(\boldsymbol{q}_{\parallel})$ finally determining the OSS cross section in Eq.(56). Such an expression is, however, not very practical, as the 2D Fourier transform in Eq.(58) has to be calculated numerically, except for the case when, $\mathcal{H} = 0.5$. Then $\tilde{g}_{ll}(r_{\parallel})$ decays in accordance with a simple exponent resulting above in Eq.(48).

Luckily, further simplification of calculations is possible due to the slit kinematics commonly applied in neutron SR and OSS measurements. Then, as was shown in the previous subsection, the integration of the OSS cross section in Eq.(56) over the azimuthal angle θ_y effectively reduces the dimension of the Fourier transform in Eq.(58) down to 1D, as in Eq.(49), while the absolute value of the vector $r_{\parallel} = \sqrt{x^2 + y^2}$ in Eq.(60) is substituted with the $x-$coordinate.

As a result, the 1D diagonal elements $\overline{\mathcal{G}}y_{ll}(q_x)$ of the 2D correlator $\mathcal{G}_{ll'}^{\parallel}(\boldsymbol{q}_{\parallel})$ integrated over θ_y are written in the form:

$$\overline{\mathcal{G}}_{ll'}^{y}(q_x) = 2|\Delta\tilde{\rho}_l|^2 \frac{\lambda \xi_{l-1} \sigma_{l-1}^2}{1 + (\xi_{l-1} q_x)^2} \delta_{ll'}, \tag{61}$$

similar to those in Eq.(48).

All these $N + 1$ interface terms, each multiplied with a combination of transmission

and reflection amplitudes, now give the explicit expression for the OSS differential scattering cross-section integrated over angles θ_y. It is clear that the contribution of each individual interface into the sum in Eq.(56) is quite small being proportional to σ_{l-1}^2, but not to ${d_l}^2 \gg \sigma_{l-1}^2$, as in Eq.(50) corresponding to defects spread through the whole layer thickness. On the other hand, the correlator $\overline{G}_{ll}^y(q_x)$ in the bulk inhomogeneity case is proportional to the concentration of those defects, which may be small, while roughness is continuous along interfaces.

The other enhancement factor of OSS from roughness is related to possible correlations of interface position fluctuations not only along a single interface, but also between different interfaces. Then the roughness contribution to OSS grows quadratically with the number of interfaces in which interface deviations are correlated. Such correlation can be taken into account via the substitution of the factor $|\Delta\tilde{\rho}_l|^2$ by the product $\Delta\tilde{\rho}_l\Delta\tilde{\rho}_{l'}$ and the factor σ_{l-1}^2 by the product $\sigma_{l-1}\sigma_{l'-1}$ in Eq.(61) and, finally, introducing the exponential factor $\exp\left(-|\overline{z}_{l-1} - \overline{z}_{l'-1}|/\xi_\perp\right)$ instead of the Kronecker symbol. This way one can describe the case when distortions of interfaces separated by a distance less than $\xi_\perp$ are conformal. If, in particular, $\xi_\perp \gg d$ then roughness distortions are conformally correlated throughout the total film thickness d and OSS is enhanced by a factor $(N+1)^2$ from all interfaces. Then, for a large number of interfaces, the OSS cross section may be quite appreciable even in the range $p_l^f\sigma_l \leq 1$ and $p_l^i\sigma_l \leq 1$. This is often the case for periodic multilayers, where OSS is additionally enhanced along the lines of constant $p_l^i + p_l^f$ corresponding to SR Bragg conditions, due to the transverse structure factor $\mathcal{G}_{ll'}^\perp(p^f, p^i)$ of the film. Further discussion of this particular case is beyond the scope of this work.

3. Representation of reciprocal space

Concluding the theoretical consideration we note that the formalism described here is self-contained in order to allow the development of fast and stable software, which is in the following efficiently applied for quantitative evaluation of data on neutron SR and OSS from a number of polymer films measured in ToF mode. The advantage of the approach is that time consuming numerical computations are reduced to a minimum by the use of theoretical models that are analytically available in the needed space. The only necessary numerical integrations are employed in the convolution of the normalized sum of SR and the OSS cross sections with the 3D resolution function of the used instrument setting and in subsequent automatic fitting of data to the result of the convolution. The least square fitting routine has been applied to raw data normalized to the neutron wavelength spectrum and collected in rectangular maps with coordinates α_f v.s. λ at fixed angle of incidence α_i.

As mentioned above, measured intensity in off-specular neutron scattering $I(p_i, p_f; q_x)$ integrated over the azimuthal angle θ_y is a function of three variables defined in Eqs. 34 and Eq. 1 in which θ_y is set to zero. Instead of these three physical quantities one can also use three other independent parameters, which are the raw instrumental ones: incoming angle α_i, outgoing angle α_f and wavelength λ. Therefore, the complete reciprocal space and thus complete information can only be acquired by varying all the three parameters. As already mentioned, two experimental techniques exist to record off-specular neutron scattering, namely the single wavelength measurement with fixed wavelength λ and the ToF mode with fixed incoming angle α_i. Only two variables are usually varied during either measurement, either α_i and α_f in the case of the first, or λ and α_f in the case of the second. Therefore the resulting maps can be plotted on a 2D grid. One should not forget, however, that these 2D maps are only projections of the 3D experimental space and therefore not unique. The features in the spectrum,

arising from the physical morphology are purely a function of q_x and vice versa, optical features are purely a function of the two wave vector projections p_i and p_f. The magnitude of q_x is particularly important, as it varies significantly and is a non-linear function of the three variables. All this combined means that the measurements of the same sample will look differently when measured at different wavelengths or incoming angles. In the case of the calculations presented above, this presents no problem, as the wavelength and the incoming angle are explicitly taken into account and all the quantities are always recalculated into the tree independent variables. However, this is important in qualitative assessment of the measurements, as the origin of the features, optics or physics, is often hardly distinguishable without a proper calculation.

One possibility to qualitatively distinguish between optical enhancements and physical structure factors is to convert the raw data into different 2D spaces (Adlmann *et al.*, 2016) and look for orthogonal intensity lines in each of them. In order to illustrate this we plot data obtained from a polymer trilayer system comprising a thin deuterated poly(methy methacrylate) (d-PMMA) film of thickness around 10 nm sandwiched between two layers of hydrogenated polystyrene (h-PS) of thickness around 150 nm (de Silva *et al.*, 2012). The top layer is dewetting by formation of holes after 110 min annealing at 160 °C. In figure 7, the same measurement is represented in three spaces (from left to right): $(\lambda, \alpha_i + \alpha_f)$, which is the raw experimental space on a ToF reflectometer, $(p_i - p_f, p_i + p_f)$, which emphasizes optical distortions and finally the most common (q_x, q_z), which emphasizes physical structure. The experimental OSS data shows a characteristic grid pattern, which is visible in all three space maps. Given the apparent periodicity of this pattern one might be tempted to qualitatively ascribe this to long-range order of the sample structure. Consequently this should produce orthogonal lines in the (q_x, q_z) representation as shown by the dashed and dotted lines in Fig. 7 right. When looking at this pattern one might be satisfied with

this conclusion. But when, on the contrary, plotting the data in $(p_i - p_f, p_i + p_f)$ space, where the lines of constant q should be highly distorted as shown by the broken lines in the middle pattern of Fig. 7 it becomes obvious that the striking features seen in the figures are optical phenomena, arising due to the interference of the neutron field inside the top layer and spaced according to the layer thickness of this layer bearing no direct information about the in-plane structure. These optical enhancements are maximized along lines of constant wave vector ($p_i - p_f$ and $p_i + p_f$) as shown as dotted lines for a very similar pattern in Fig 9, which is discussed later. Another conclusion from the fact that intensity lines along constant $p_i \pm p_f$ are present is that there must be "bulk" defects present in the top layer as predicted by Fig, 4. If only roughness correlation was causing OSS then those lines would be missing as illustrated in Fig. 6. This was indeed the case for this sample as holes crossing the top layer were identified here by several microscopy techniques (not shown).

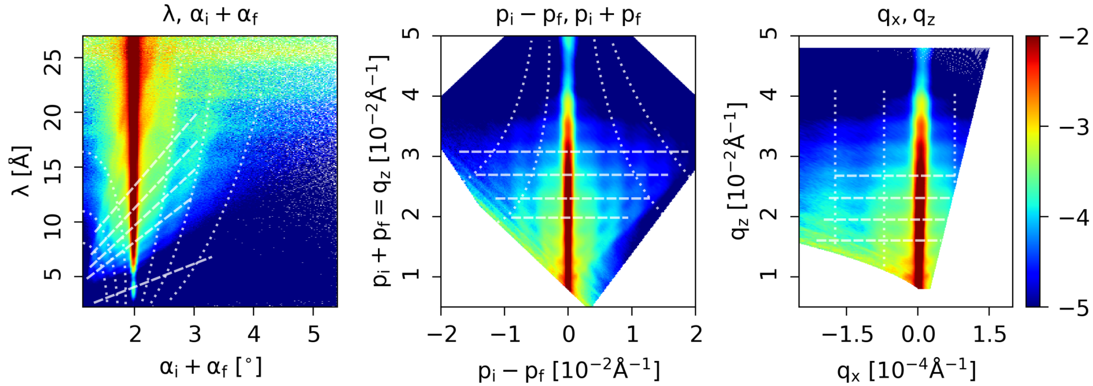

Fig. 7. Plots of a trilayer system in three different representations: left $(\lambda, \alpha_i + \alpha_f)$, center $(p_i - p_f, p_i + p_f)$, and right (q_x, q_z). These representations are discussed in the text. In the plots the dashed lines show constant q_z and dotted lines show constant q_x. The lines illustrate the features of the off-specular scattering signal arising from physical correlations.

4. Comparison with experiments

We have used the combined SR and OSS presented in the previous sections to characterise soft systems which present less defined structures and interfaces if compared to solid state materials. These aspects constitute a supplementary level of complexity in the OSS signal analysis. In particular, we have investigated thin polymer films and the presence of instabilities of the systems. In some cases dewetting via the nucleation process was observed with OSS originated in different positions of the sample structure. Samples comprising either two or three immiscible thin polymer layers deposited onto a silicon substrate were used.

As described in the theoretical section two types of interface structure leading to OSS are described in this work: i) interface roughness correlated both in-plane, with one interface, and out-of-plane between interfaces, and ii) inhomogeneities in the SLD inside the layers.

Concerning i), the polymer-polymer roughness can be decomposed into an intrinsic interface width determined by Self Consistent Field theory, related to the Flory-Huggins interaction parameter between the two polymers and their monomer sizes which is not giving rise to OSS, and a contribution stemming from thermal fluctuations, i.e. capillary waves (Sferrazza *et al.*, 1997), giving rise to OSS. For a more simple approach, we will assume that all the roughness determined by SR will give rise to OSS as mentioned above, and hence we will not distinguish those two contributions for the sake of clarity. An approach to identifying these different mechanisms has been presented elsewhere (James *et al.*, 2015).

For some cases the off-specular scattering originating from the polymer/polymer interfaces was overshadowed by the OSS from case ii), namely nucleation of holes of the layers that took place on the top of the film or in the buried polymer layer, as we will show later.

Since our goal is to apply the OSS technique to various situations to illustrate the power of the approach for the study of hidden interfaces, bilayers of immiscible polymer films were prepared and measured after the systems were annealed above the glass transition temperature (Tg) of the polymers (Tg is around 100 - 110 °C for the two polymers). As materials, we used 150 nm to 360 nm thick poly(methyl-methacrylate) (PMMA) layers on top of thin (10 nm to 15 nm) polystyrene (PS) deposited on polished silicon wafers.

From a polymer physics point of view, the instability of thin films may proceed via spinodal dewetting (Brochard-Wyart & Daillant, 1990; Xie *et al.*, 1998; Higgins & Jones, 2000), driven by dispersive long-range van der Waals interactions (Reiter *et al.*, 1999; Seemann *et al.*, 2001*a*; Seemann *et al.*, 2001*b*), or via a nucleation process (Reiter, 1992; Bischof *et al.*, 1996; Sharma & Reiter, 1996; Jacobs *et al.*, 1998; Geoghegan & Krausch, 2003).

If a layer in the system is unstable due to any of the above reasons, it will eventually dewet (the film will break down and form droplets at the final stage) when heated above Tg. The instability can increase spontaneously via a spinodal type process (de Silva *et al.*, 2007) if van der Waals forces are unfavorable for example, or nucleation can take place (Jacobs *et al.*, 1998) if the spreading coefficient is negative (De Gennes, 1985). If both criteria of instability are met one or the other will start earlier depending mainly on the density of nucleation sites or other inhomogeneities present in the film (Pototsky *et al.*, 2005). Note that nucleation seeds can also occur due to sample preparation - presence of inhomogeneities due to film preparation and spin coating, where stress can induce plastic deformation (Richardson *et al.*, 2003).

In the cases studied here, we will use chemically untreated silicon surfaces representing a rather low surface energy. It has been shown that for thin polymer films deposited on low-energy surfaces, leading to a negative spreading coefficient, heterogeneous nucle-

ation due to subtle density inhomogeneities inside the polymer, will start and destroy the film before any spinodal type process can occur (Jacobs *et al.*, 1998). This was indeed observed for two out of the three sets of samples presented here.

For the purpose of the discussion we divided the systems into three cases, depending on the final observation:

Case A) Dewetting of the top layer: for this case we have used bilayers composed of a thin layer of deuterated polystyrene (d-PS) of thickness less than 15 nm cast on the Si substrate with a capping film of protonated PMMA (h-PMMA) of around 150 nm.

Case B) Dewetting of the buried film: a bilayer system composed of a thin layer of d-PS of thickness less than 15 nm in contact with the silicon substrate with a thicker capping layer of h-PMMA of around 360 nm.

Case C) No holes observed: a bilayer system composed of a thin layer of deuterated polystyrene (d-PS) of thickness less than 15 nm on a silicon substrate with a thicker capping layer of h-PMMA of around 300 nm.

4.1. Experimental details

The silicon substrates are 5 cm diameter and 0.5 cm thickness. One side was polished and had a native oxide layer (SiO_2) of thickness of around 2 nm and a roughness of around 0.5 nm. The thickness of the SiO_2 was measured with ellipsometry (Beaglehole Picometer and Horiba spectroscopic M16) prior the polymer deposition. The surfaces were cleaned by ultrasonication in several organic solvents and Milli-q water, leading to a surface energy of $26\,mJ/m^2$ (Liesche, 2012).

The first polymer layer was spin coated from a toluene solution; for a bilayer system the second layer was first spin coated onto a glass slide and, after the floating process, was deposited onto the first layer. For the trilayer system shown in Sec. 3, since the

thickness of the thin d-PMMA film was very small, the floating was problematic in order to get an uniform layer. We therefore deposited this layer directly onto the first layer via spin coating from an acetic acid solution, and after, the third layer was floated and deposited. The spin coating of the second layer ensured a good quality trilayer system as was clearly visible from the refelctivity profiles, which showed the Kiessig fringes originated from this thin d-PMMA layer. For this trilayer system the molar mass (Mw) was 630 kDa for the h-PS and 53 kDa for the d-PMMA: this allowed a viscosity match for the two polymers. For the bilayer systems different combinations of Mw were used as stated in the text. All the thicknesses were characterized with a spectroscopic or a laser ellipsometer.

The samples were then annealed above Tg in a vacuum oven at $T = 160\,°\mathrm{C}$ for different times and then quenched back to room temperature for the neutron scattering experiments. Spin-coating was done on a Delta6 Süss MicroTec spinning at 500 rpm for 2 s, followed by 3000 rpm for 55 s. The target layer thickness was achieved by varying the polymer concentration of the deposited solution.

The kinetics of the interface formation and eventually of the breakup process of the layer was monitored as a function of the annealing time with both SR and OSS that were performed on the D17 reflectometer in ToF mode (Saerbeck *et al.*, 2018) at the Institut Laue-Langevin. For SR the relative wavelength resolution $\Delta\lambda/\lambda$ and angular divergence $\Delta\alpha_i/\alpha_i$ were both fixed at 1%, whereas for OSS $\Delta\lambda/\lambda$ was varied between 1% and 4% in the investigated q-range and $\Delta\alpha_i/\alpha_i$=1.5%. All resolutions are given in FWHM. In both cases the foot print on the sample was fixed to a square of 30 mm $\times$ 30 mm. The detector was 3.1 m away from the sample and had a pixel size of 1.2 mm in the relevant direction. SR data was normalized to the incident beam spectrum by using COSMOS (Gutfreund *et al.*, 2018) and OSS data were normalized by using LAMP (Richard *et al.*, 1996) and transformed into q or p space by using Överlåteren

(Adlmann *et al.*, 2016) if needed for visualization. OSS fitting was done in λ vs. 2θ space using the here described algorithm. SR fitting was done in q-space with the here presented algorithm.

Complementary atomic force microscopy (AFM) images were acquired on an Asylum Research MFP-3D in tapping mode. The size of scans was $50\,\mu$m $\times$ $50\,\mu$m using a 512 $\times$ 512 grid of square points with a size of 97 nm.

4.2. Instability of the top layer (Case A)

The systems were prepared as described above and were annealed up to 120 minutes at 160 °C. The d-PS layer (Mw= 66 kDa had a thickness of $d_{\text{d-PS}} = 155\,\text{Å}$, while the h-PMMA had a molar mass of Mw= 298 kDa and a thickness of $d_{\text{h-PMMA}} = 1700\,\text{Å}$. The SR for the bilayer system (DW4) obtained at the different annealing times are shown in figure 8.

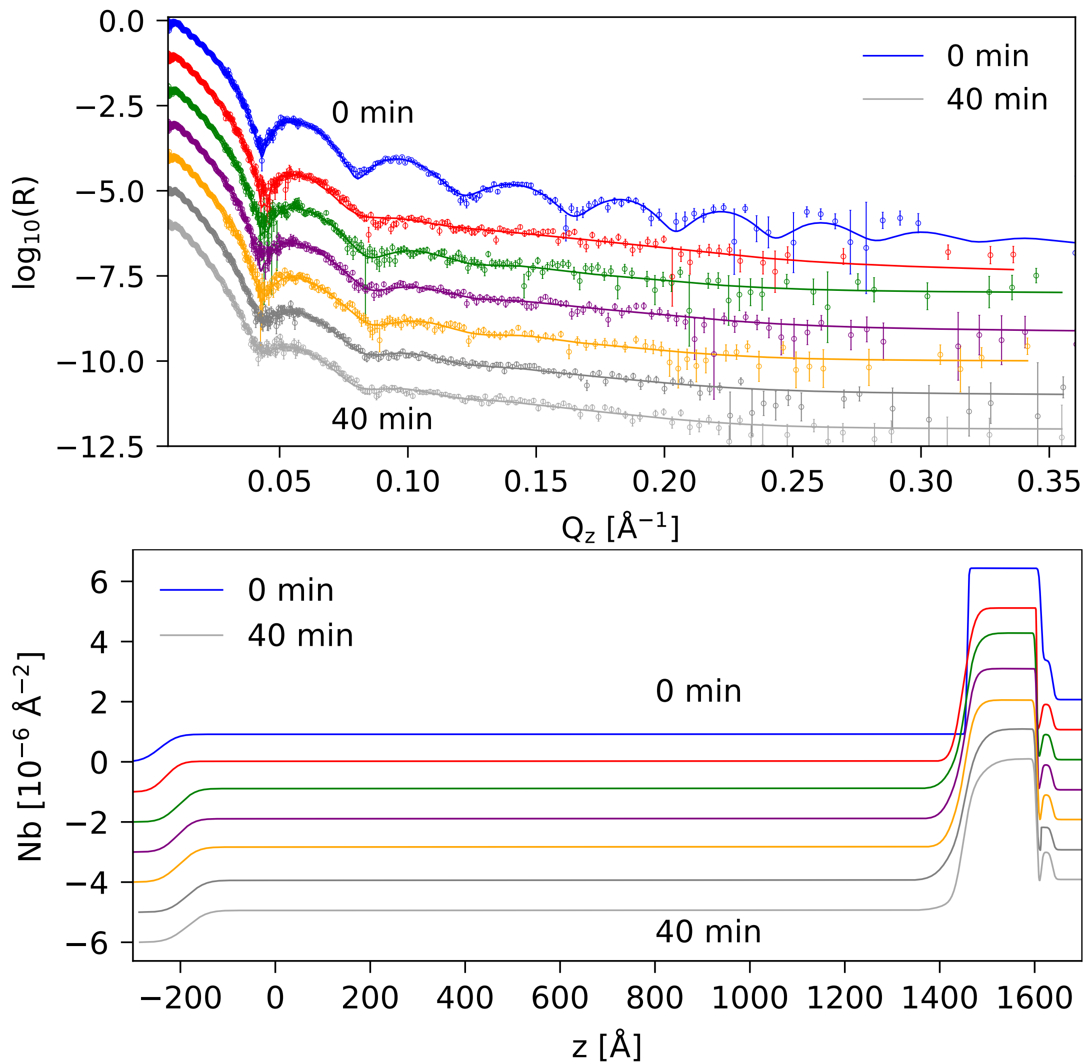

Fig. 8. Top: Reflectivity of the DW4 PS/PMMA bilayer sample with thin capping layer, annealed profiles are shifted by factors of 10 for clarity. Bottom: SLD of the DW4 PS/PMMA bilayer sample with thin capping layer, annealed profiles are shifted by factors of 10 for clarity. Exact annealing times from shortest to longest: 0 min, 10 min, 15 min, 20 min, 25 min, 30 min, 40 min.

The SR curves were fitted with 2 different models. For short annealing times, the system can be fitted with a 3-layer model: h-PMMA / d-PS / SiO_2. The initial fit at $t = 0$ min shows the system as it is, after deposition. Many well-defined Kiessig fringes, coming from both the thin and thick layers, can be seen, showing a good

homogeneity of the sample. The roughness between the layers is initially also small, $\sigma \sim 5$ Å. Annealing the sample, we can immediately see an increase in the roughness at the polymer-polymer interface, as the well-defined Kiessig fringes start to disappear. Eventually, they are completely gone, signifying a complete rupture of the buried layer. After the second annealing step at $t = 15$ min, in order to maintain the quality of the fit as before, a 4th layer must be introduced with a thickness d_{inter}. It represents the extended interfacial region, which is a mixture between the d-PS and h-PMMA. This signifies the beginning of a breakup of the bottom layer and simultaneously the dewetting of the top layer.

For all further steps until $t = 40$ min, the 4-layer model can be used and the mass conservation in the fits is strictly obeyed. However, when annealing 90 min or longer, the sample cannot be fitted well with such a model anymore. We consider it to be in a completely dewetted state, as the Kiessig fringes are completely gone and therefore cannot be fitted with a simple slab model anymore.

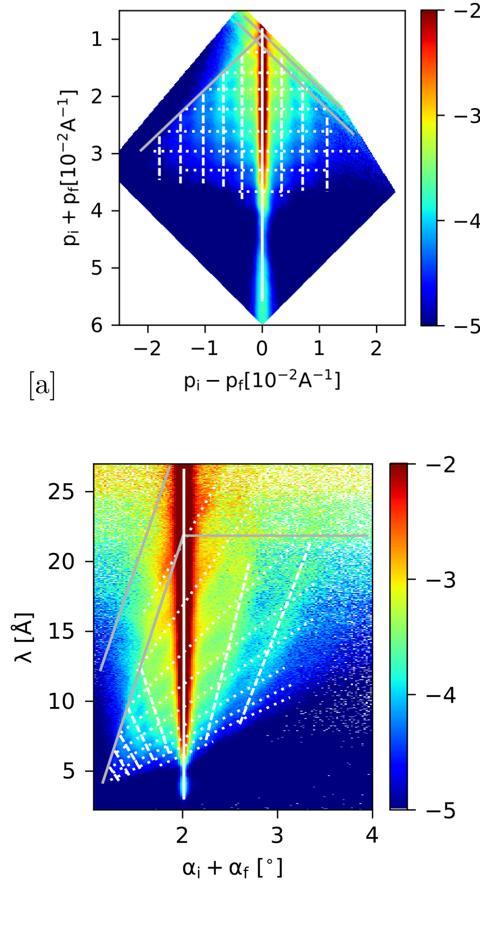

Fig. 9. Sample Case A: Scattering features in (a) $(p_i - p_f, p_i + p_f)$ and (b) $(\lambda, \alpha_i + \alpha_f)$ space. White dotted lines mark features arising from the interference between the bottom and the top interface and are spaced according to the thickness of the top layer. Dashed white lines represent features caused by the interference of the neutrons, due to the holes present in the top layer. Their spacing is the same as for the dotted white lines. Gray solid lines mark Yoneda peaks of different materials, namely Si and h-PMMA. d-PS is not seen, as it is too thin in this example. The vertical white solid line corresponds to the specular ridge.

A typical OSS measurement of this system is shown in Fig. 9. A qualitative analysis of the spectrum reveals a grid-like structure when transformed into $(p_i - p_f, p_i + p_f)$ space (see Fig. 9) indicating optical enhancements due to bulk defects as explained in relation to Fig. 4. The spacing of these enhanced intensity lines corresponds to the thickness of the top h-PMMA layer giving a hint on the location of the SLD deviations giving rise to this enhancement. Indeed, the interference of neutrons inside this layer is visible as parallel vertical lines at constant $p_i - p_f$ marked as dashed lines

in the figure. The dotted parallel lines at constant $p_i + p_f$ represent features due to the interference between the top and bottom interface of the h-PMMA and have the same spacing as the Kiessig fringes coming from this layer in SR. In essence, from the qualitative analysis of the OSS map it becomes clear that the top h-PMMA layer bears significant SLD inhomogeneities giving rise to these scattering enhancements. This can be explained by the gradual appearance of holes in this layer as can be seen in complementary AFM pictures taken at later annealing time (Figure S4 in the SI). We note here that SR was not able to detect the presence of these holes since their small concentration (at the start of the process) in the protonated polymer (surface fraction $< 5\%$) does not change the SLD in specular reflectivity within the experimental error. Therefore, although the OSS enhancements in p_i, p_f space are purely optical phenomena and, in theory, do not carry any quantitative information beyond that already obtained by specular fits, the sensitivity of small SLD variations may be well beyond that of SR and thus could act as an additional scattering contrast in the co-refinement of SR data, especially for thick films.

Hence, the features marked by the parallel dashed lines at constant $p_i - p_f$ are caused by the interference of neutrons inside the top layer due to holes filled with air. As can be seen in ref. (James *et al.*, 2015), such lines are not visible in stable bilayers, where only the constant $p_i + p_f$ lines are present.

In order to quantitatively fit the OSS patterns we used the SR fitting results for the sample stratification and the following contributions to the OSS. As already mentioned, the two shortest annealing times are fitted with a 3-layer model: h-PMMA on d-PS on SiO_2 on Si. For those samples the only source of perturbation, and thus contribution to the OSS, is the growth of the holes in the top layer (not for the initial film) and the correlated roughness at the interface between the two immiscible polymers. As we further anneal the system, the OSS intensity grows and, just as in

specular reflectivity, a 4-layer model is needed, with the majority of OSS scattering intensity coming from the larger and larger scattering volume of the extended interfacial region between the two polymer layers. Furthermore, the holes in the top layer are growing and are the dominant contribution to the spectrum. The OSS measured and calculated intensities for 40 min annealing times is shown in Fig. 10

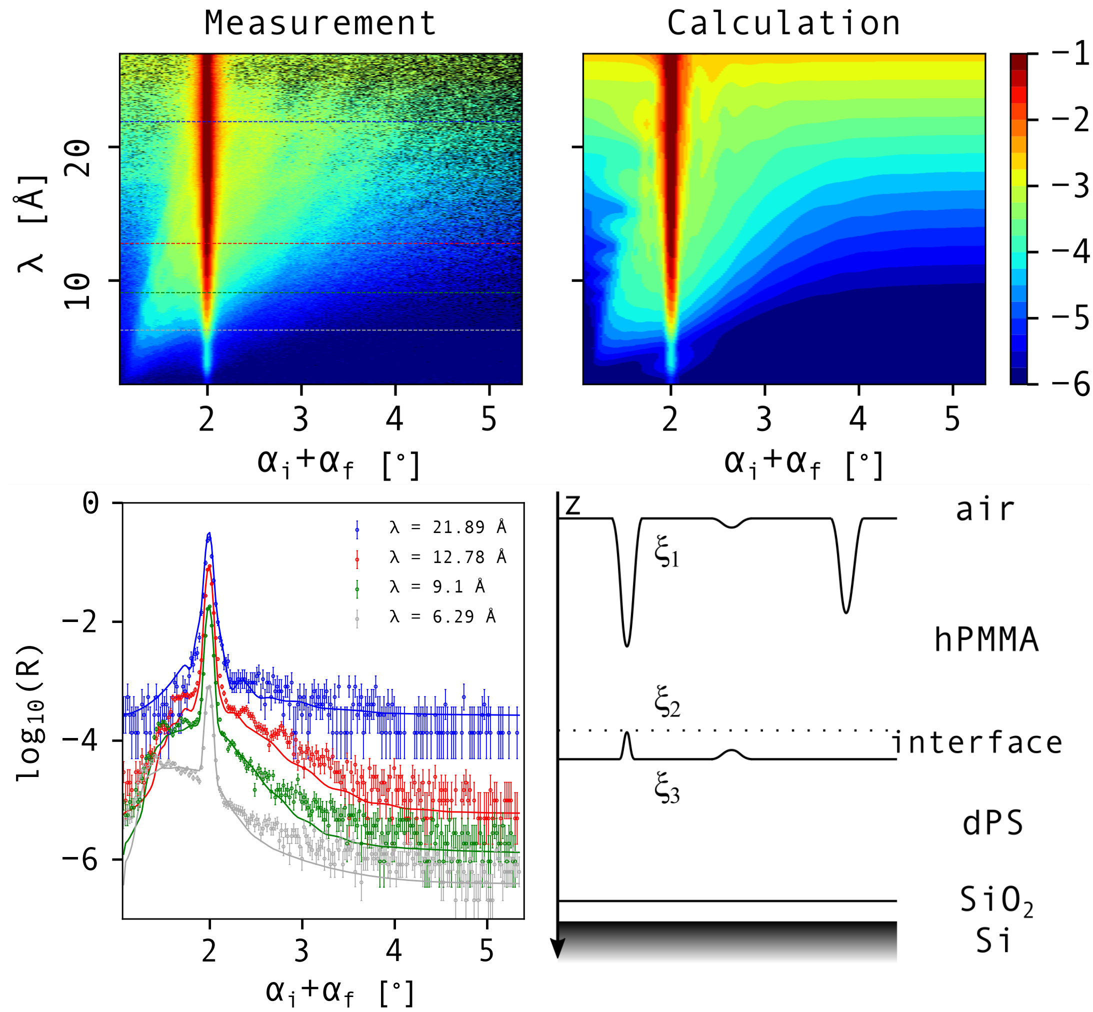

Fig. 10. Measurement and DWBA calculation for $t = 40$ min annealed sample Case A in the $(\alpha_i + \alpha_f, \lambda)$ space. Below left: 1D cuts at different wavelengths indicated in the legend. Bottom right: schematic of the model. ξ_1 corresponds to the size of holes inside the h-PMMA layer and the in-plane correlation length of the roughness of the h-PMMA surface (both values kept the same), while ξ_2 corresponds to the in-plane correlation length of the roughness at the interface between the h-PMMA and the interfacial layer (dotted line) and the size of craters inside this layer (both values kept the same). ξ_3 corresponds to the in-plane correlation length of the roughness at and the interface between the interfacial layer and the d-PS.

In order to simulate this OSS pattern, we model the following distinct contributions: first, the top layer is modelled with holes penetrating the whole layer, by assuming an exponential in-plane correlation function, with a correlation length ξ_1 corresponding roughly to the hole radius. The SLD contrast for the OSS in this layer is that between pure h-PMMA and air. Since a small concentration of holes (surface fraction $< 5\%$) would change the SLD in specular reflectivity only within the experimental error, the concentration c_h of holes inside the layer was used as a free fitting parameter in contrast to all other inhomogeneity fractions that were deduced from the SLDs of the SR fits. Secondly, in the first two annealing steps, the only other contribution is the correlated roughness at the interface between the h-PMMA and d-PS, which is also assumed to follow an exponential in-plane decay with a correlation length ξ_2. In all the other annealing steps, an additional interfacial layer between the two polymers is used to fit the specular reflectivity and this whole layer is also source of perturbation giving rise to off-specular scattering. This is also modeled with an exponentially decaying in-plane correlation length ξ_3 with the SLD contrast coming from that of pure d-PS and pure h-PMMA. An overview of all fitting parameters is given in table S1 in the SI.

4.3. Dewetting of the buried layer (Case B)

Two other bilayer systems, similar to Case A, but with a thicker top h-PMMA layer were prepared to minimize an eventual influence of the free interface on the underlying buried polymer-polymer interface and, in particular, suppress the appearance of holes in the h-PMMA. One of the samples, discussed in this section, already initially had a lower-than-nominal SLD for the bottom thin layer, namely $\rho_{\text{dPS}} = 5.5 \times 10^{-6}\,\text{Å}^{-2}$, probably connected to a dewetting process. Its thickness was determined to be $d_{\text{d-PS}} = 107\,\text{Å}$ and molar mass: 60 kDa. It still serves as a very good demonstrator of the DWBA OSS formalism developed here, as even a relatively unknown morphology can

be investigated and identified with the proposed workflow for the analysis. This layer was capped with a $d_{\text{h-PMMA}} = 3627\,\text{Å}$ thick PMMA layer (Mw=310 kDa).

The sample was first measured as prepared and then annealed in 5 min steps at $T = 160\,^{\circ}\text{C}$. Annealing the sample, the evolution of the layer breakup is clearly visible (see figure 11), as the specular fringes connected to the thin bottom layer start to disappear due to the increase in d-PS/h-PMMA interfacial width, as seen in the density profile of the bottom figure. At the same time, the SLD of the bottom layer further decreased.

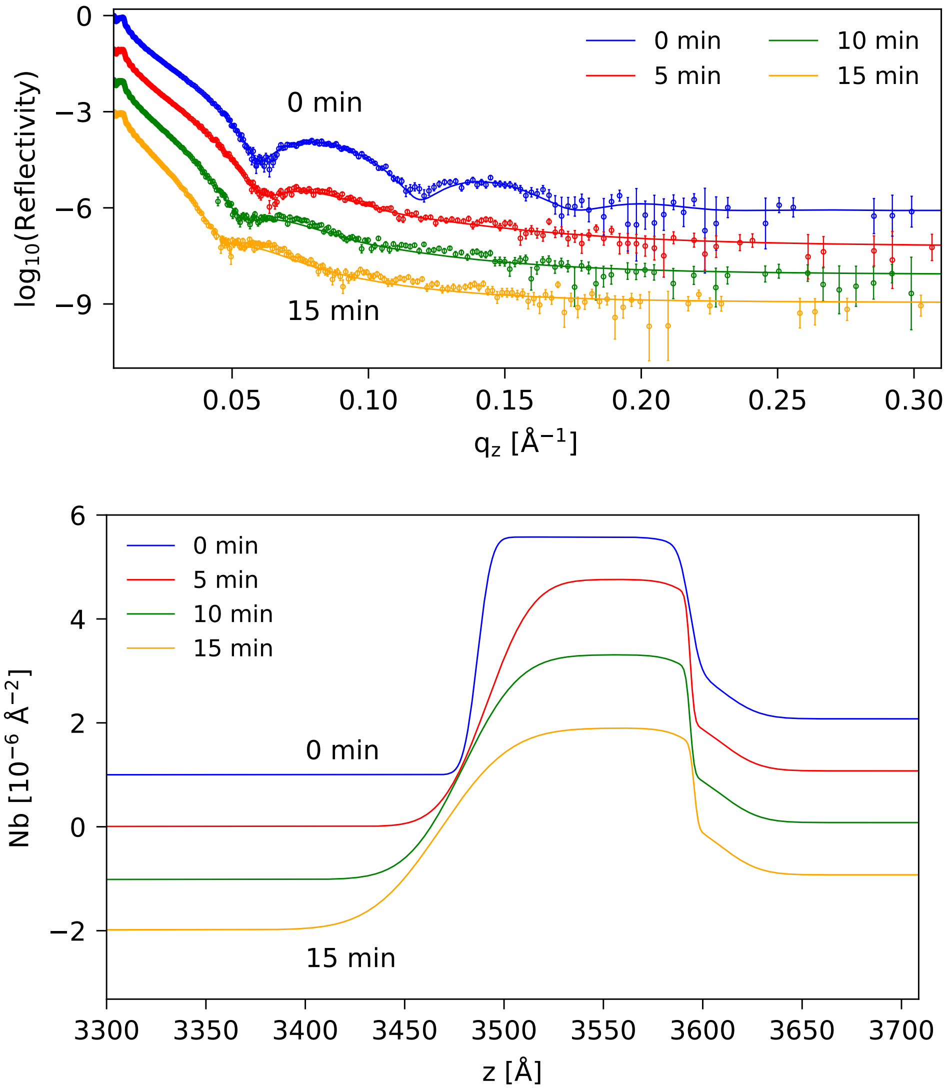

Fig. 11. Top: NR data (points) and fits (lines) of the bilayer with a thick capping layer (Case B) for different annealing times as indicated in the legend. Bottom: SLD profiles of the NR fits in the same color code. The NR and SLD values for the annealed samples are offset by factors of 10 for clarity.

Considering the model for the OSS simulation, we clearly observe the absence of the grid-like pattern since the top layer is now not dewetting. Hence the Yoneda-type scattering (similar to the one observed previously) may come from instability of the bottom film (de Silva *et al.*, 2009).

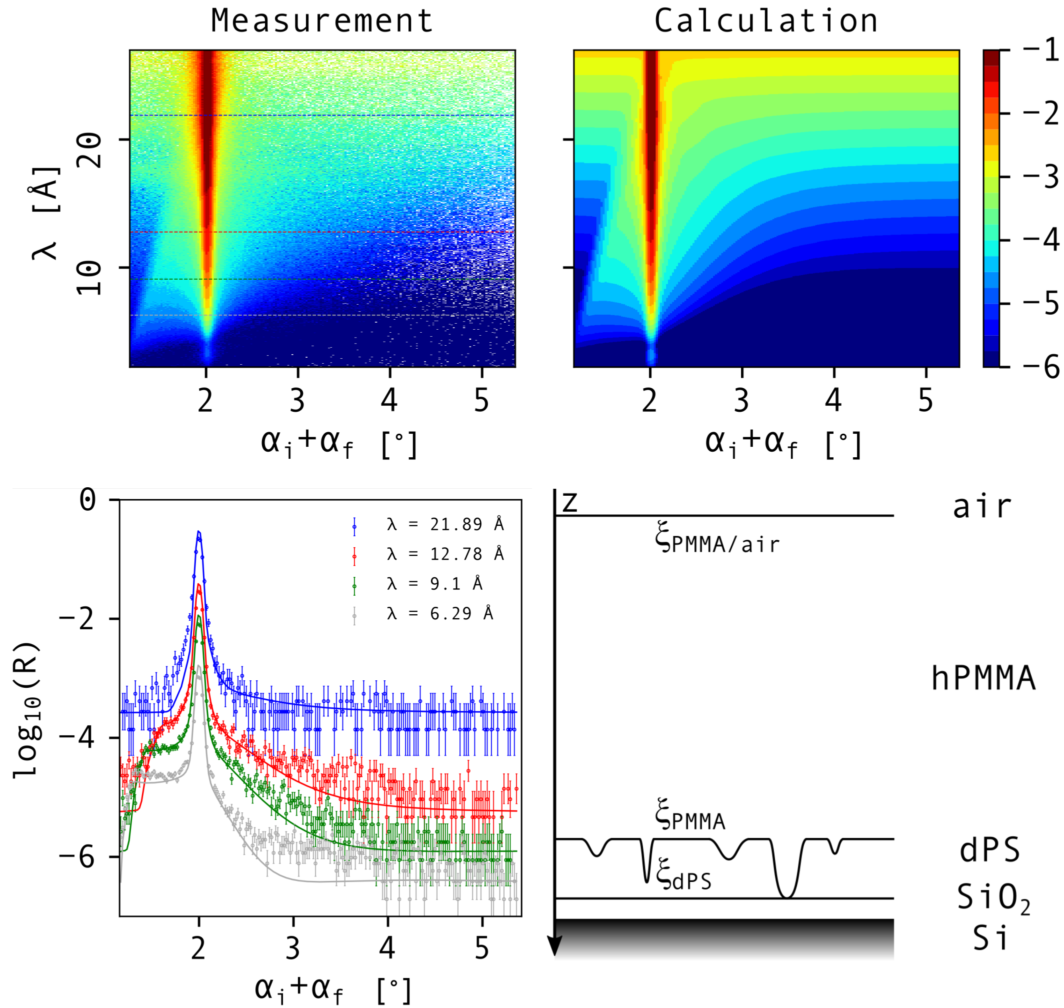

Fig. 12. OSS experimental data (top left) and simulation (top right) of the Case B sample in $(\lambda, \alpha_i + \alpha_f)$ space, $t_{\text{annealing}} = 10\,\text{min}$. Bottom left: 1D cuts at different wavelengths as indicated in the legend. Bottom right: schematic of the model. $\xi_{\text{PMMA/air}}$ corresponds to the in-plane correlation length of the roughness of the h-PMMA surface, ξ_{PMMA} corresponds to the size of the holes filled with h-PMMA inside the d-PS layer and ξ_{dPS} corresponds to the size of the d-PS phases in between.

Consequently, for the modelling of the OSS, we consider a homogeneous h-PMMA layer, not giving rise to OSS and a thin bottom d-PS layer assumed to be composed of two domains, h-PMMA and d-PS, respectively, contributing to OSS. In total there are 3 different sources of OSS modeled that contribute to the total scattering spectrum: The correlated air/h-PMMA roughness (with a correlation length $\xi_{hPMMA/air}$), h-

PMMA domains and d-PS domains within the bottom layer, all of them decaying exponentially. Each of the contributions has its own contrast. Constructing the model, we assume that the bottom layer comprises laterally phase-separated domains (which is a reasonable assumption, given that PS and PMMA are immiscible) following the Ansatz presented in the SI. As the concentration of h-PMMA inclusions in the d-PS layer is rather high we assume that both domains exhibit a mean size and fit two independent correlation lengths ξ_{PMMA} and ξ_{PS}, where the first represents the average size of the *holes* filled with h-PMMA and the second the average size of the d-PS *droplets*. In accordance to eq. S6from the SI we get the following pair correlator for the d-PS layer:

$$\begin{aligned} G^{\|}(\boldsymbol{q}_{\|}) = c|\rho_{\text{d-PS}} - \overline{\rho}|^2 \langle |F_{\text{d-PS}}(\boldsymbol{q}_{\|})|^2 \rangle + \\ (1-c)|\rho_{\text{h-PMMA}} - \overline{\rho}|^2 \langle |F_{\text{h-PMMA}}(\boldsymbol{q}_{\|})|^2 \rangle + \\ c(1-c)(\rho_{\text{d-PS}} - \overline{\rho})(\rho_{\text{h-PMMA}} - \overline{\rho}) \langle F_{\text{h-PMMA}}(\boldsymbol{q}_{\|}) F_{\text{d-PS}}(-\boldsymbol{q}_{\|}) \varepsilon(q_{\|}) \rangle, \end{aligned} \tag{62}$$

with c and $(1-c)$ being the d-PS and h-PMMA volume fractions in the layer, respectively, and $\overline{\rho}$ being the SLD obtained from the specular fit. The cross-position correlation function $\varepsilon(q_{\|})$ is assumed to be a Lorentzian with a correlation length corresponding to the average between the d-PS and h-PMMA correlations: $\xi_{\text{cross}} = \frac{\xi_{\text{PMMA}} + \xi_{\text{PS}}}{2}$. This way, a minimum number of parameters is required as the volume fraction are defined as:

$$c = \frac{\overline{\rho} - \rho_{\text{h-PMMA}}}{\rho_{\text{d-PS}} - \rho_{\text{h-PMMA}}}\,, \tag{63}$$

with $\rho_{\text{d-PS}} = 6.407 \times 10^{-6}\,\text{Å}^{-2}$ and $\rho_{\text{h-PMMA}} = 1.059 \times 10^{-6}\,\text{Å}^{-2}$ being the nominal SLDs of the polymers.

Estimating the initial c of d-PS in the layer following equation S3 from the SI:

$$c = \frac{5.5 \times 10^{-6}\,\text{Å}^{-2} - 1.059 \times 10^{-6}\,\text{Å}^{-2}}{6.407 \times 10^{-6}\,\text{Å}^{-2} - 1.059 \times 10^{-6}\,\text{Å}^{-2}} = 0.83\,, \tag{64}$$

it can be seen that the two phases, the d-PS and h-PMMA respectively, contribute almost equally, as the d-PS contrast with the mean SLD is lower than that of the h-PMMA. Examining now the fits of off-specular scattering, shown in Figure 12 for 10 min annealing time, together with the measurements, it can be seen that the model reproduces the results. An overview of all fitting parameters is given in table S2 in the SI.

4.4. Bilayer system with no dewetting (Case C)

For the second system mentioned above, no nucleation in any layer was observed. The SLD of the buried d-PS layer (Mw=60 kDa) was close to nominal and its thickness was 114 Å, capped with a thick h-PMMA layer (3000 Å), screening possible effects of the free surface on the buried interface. The SR data (see figure 13) show the characteristic fringes of the d-PS film and the profile illustrates an increased d-PS/h-PMMA interface upon annealing: The roughness increases to 24 Å after 10 minutes annealing. After this first annealing step, no considerable d-PS SLD drop is observable, indicating that the layer is still homogeneous. Such behavior of the observed SLD profile signifies that the layers are still homogeneous and only the thermal fluctuations at the interface are growing, pointing to either the film stability or an early stage of spinodal dewetting. In such case, one should not detect noticeable change in the SLDs of the layers, but only the increase in interfacial roughness (Sferrazza *et al.*, 1998).

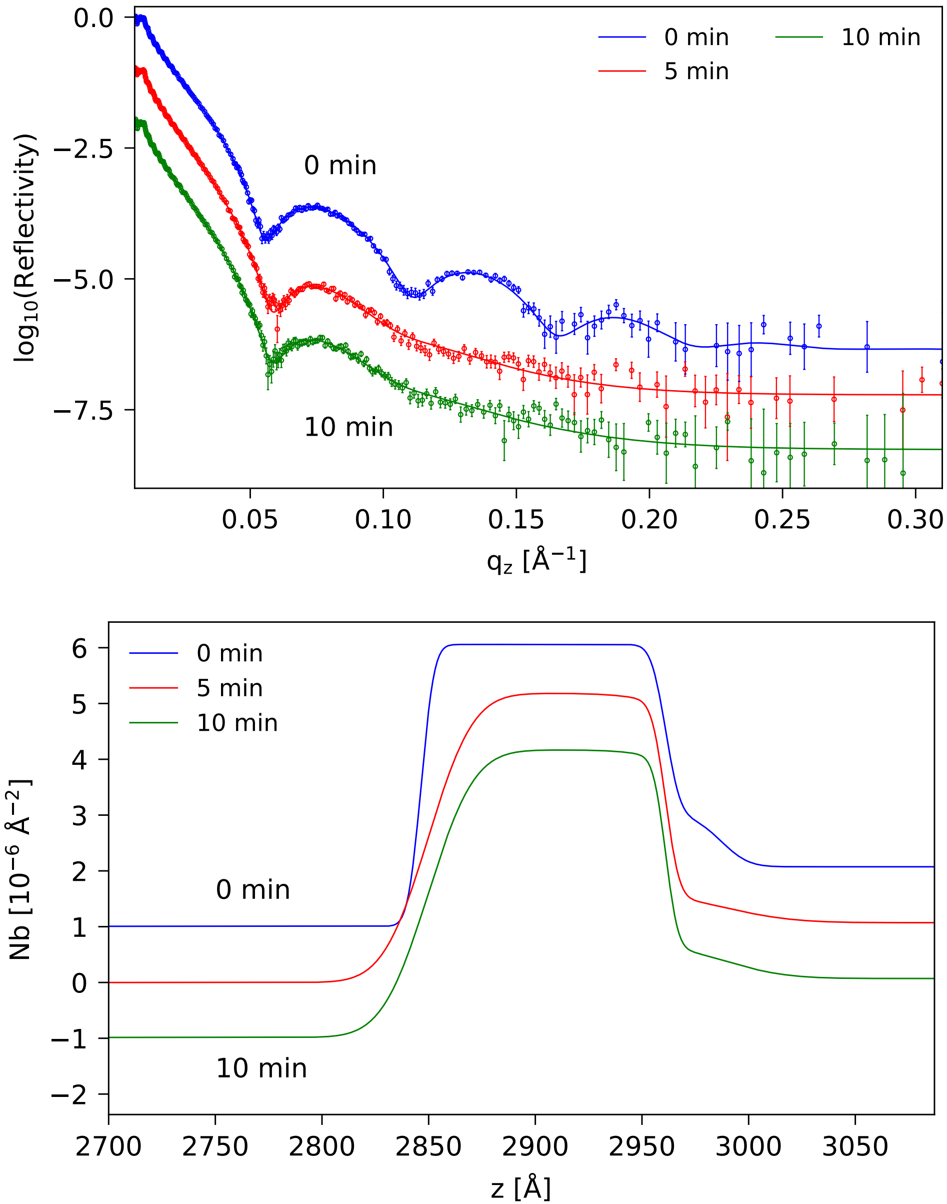

Fig. 13. Top: NR data (points) and fits (lines) of the bilayer with a thick capping layer (Case C) for differet annealing times as indicated in the caption. Bottom: SLD profiles of the NR fits in the same color code. The NR and SLD values for the annealed samples are offset by factors of 10 for clarity.

The OSS pattern for 5 min annealing time is shown in figure 14. We can observe that there is no characteristic grid-like structure on the scattering indicating that holes are not present for this systems. Rather than any regular structure appearing, there

is a change in the diffuse spectrum. The only source of OSS in the simulation is the in-plane correlated roughness at the h-PS/d-PMMA interfaces with an exponentially decaying correlation length $\xi_{PS/PMMA}$. The data are well reproduced as visible from the plot and the cut of figure 14. All fit parameters are summarized in Tab. S3in the SI.

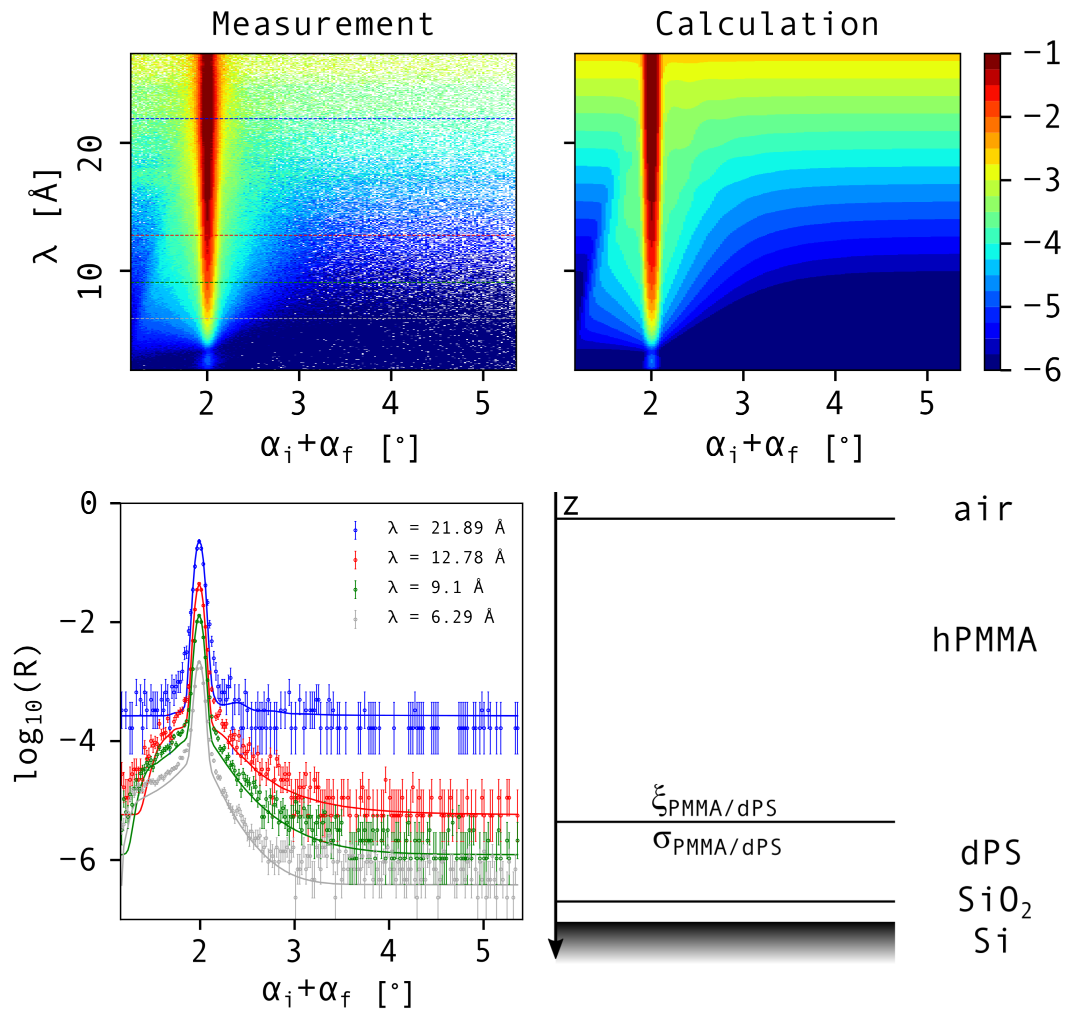

Fig. 14. Top: OSS measurement (left) and calculation (right) for the Case C sample in $(\lambda, \alpha_i + \alpha_f)$ space, $t_{\text{annealing}} = 5\,\text{min}$. Bottom left: The corresponding 1D cuts at different wavelengths as indicated in the legend. Bottom right: schematic of the model. $\xi_{\text{PMMA/dPS}}$ corresponds to the in-plane correlation length of the roughness at the polymer/polymer interface, while $\sigma_{\text{PMMA/dPS}}$ corresponds to the out-of-plane width of this interface.

5. Conclusion

Full reflectometry, a combination of specular reflectivity and off-specular scattering, is a technique which yields quantitative information of the 3D structure of the buried interfaces. Features of length scales spanning several orders of magnitude (from $\sim$ Å to $\sim 10\,\mu$m) can be observed simultaneously. Combined with the neutron properties, which are favorable for soft matter research, this makes it a unique tool for *in situ* non-destructive investigations. However, due to its nature, the technique can only be exploited to its full potential by using an advanced analysis workflow, consisting of robust data reduction and manipulation routines, and advanced analysis methods. Besides the low neutron flux and 2D detectors, the lack of suitable analysis tools has significantly held the usage back for more complex systems. The tools that have been developed in this work are intended to make off-specular analysis more available. Moreover, they have been backed by experimental validation on model thin polymer systems. The following was achieved and thoroughly described in this work:

- Implementation and experimental verification of a specular reflectivity Parratt's recursive algorithm, allowing for a robust calculation of amplitudes of upward and downward moving neutrons inside the sample. This is particularly important in soft matter, as the SLD structure (due to deuteration) often has interchanging high and low SLD layers, which causes numerical instability if using common implementations of the algorithm found in literature.
- Derivation and verification of the off-specular differential scattering cross-section, including low roughness approximation and perturbation located throughout the layer. Implementation of the findings in a multilayer calculation algorithm with as few free parameters as possible, similar to specular reflectivity. An exponential decay of the correlation function in real space has been shown as a very good approximation to the experimental results analyzed here. The calculation

is done in the experimental $(\lambda, \alpha_i + \alpha_f)$ space, due to the minimum amount of convolution steps being involved to properly implement resolution.

- Scaling of specular reflectivity to off-specular scattering for time-of-flight instruments, enabling both the calculation of off-specular scattering intensity in absolute units and simultaneous fitting of specular and off-specular parts. This gives the ability to not only analyze, but also predict scattering patterns and the location and intensity of expected features in advance.
- It is shown that the routines that were developed for transformation between different representations of reciprocal space allow for qualitative (pre-)inspection of the data. Features dependent on the structure appear parallel in (q_x, q_z) space, as the form factor is a function of the lateral wavevector q_x. Features dependent on the interference of neutrons inside the sample, arising from the complex SLD structure, which is very common in soft matter (e.g. interchanging high and low SLD), are parallel/orthogonal in $(p_i - p_f, p_i + p_f)$ space and are purely due to optical enhancements along constant wave vector combinations. It is shown that parallel intensity lines correspond to "bulk" defects inside the layers, whereas orthogonal lines (constant $p_{i/f}$) indicate correlated roughness in between the layers.
- Verification of the above-mentioned algorithms on experimental data from various Si/PS/PMMA bilayer samples. In particular, the strength of combining specular and off-specular analysis revealed the presence of holes in some PMMA capping layers, which would not have been visible by specular analysis only. The appearance and growth of holes in the buried PS layer, not directly accessible by microscopy, was followed quantitatively. Finally, the in-plane correlation length of the buried polymer/polymer roughness was extracted as a function of annealing time.

Acknowledgements

This work was supported by the Fonds de la Recherche Scientifique - FNRS Grant n. J.0103.17. The authors thank also BELSPO of Belgium for supporting the PhD studentship of A.H. via the participation of Belgium to the ILL. We are also grateful for the beam time allocation on D17 (https://doi.ill.fr/10.5291/ILL-DATA.9-11-1783, https://doi.ill.fr/10.5291/ILL-DATA.9-11-1841 and https://doi.ill.fr/10.5291/ILL-DATA.9-11-1842). We thank the PSCM for complementary measurements, notably AFM.

References

Adlmann, F. A., Pálsson, G. K., Bilheux, J., Ankner, J., Gutfreund, P., Kawecki, M. & Wolff, M. (2016). *Journal of Applied Crystallography*, **49**(6), 2091–2099.

Bischof, J., Scherer, D., Herminghaus, S. & Leiderer, P. (1996). *Physical review letters*, **77**(8), 1536.

Brochard-Wyart, F. & Daillant, J. (1990). *Canadian Journal of Physics*, **68**(9), 1084–1088.

Castel, A., Gutfreund, P., Cabane, B. & Rharbi, Y. (2020). *Langmuir*, **36**(42), 12607–12619. PMID: 33044083.
URL: *https://doi.org/10.1021/acs.langmuir.0c02162*

Cowley, J. M. (1950). *Journal of Applied Physics*, **21**(1), 24–30.

Cowley, R. (1987). *Phase transitions in Neutron Scattering: Methods of Experimental Physics*. Academic Press, Inc.

Daillant, J. & Belorgey, O. (1992). *The Journal of Chemical Physics*, **97**(8), 5824–5836.
URL: *http://link.aip.org/link/?JCP/97/5824/1*

Daillant, J. & Gibaud, A. (eds.) (2009). *X-ray and Neutron Reflectivity - Principles and Applications*, vol. 770 of *Lect. Notes Phys.* Heidelberg: Springer.

De Gennes, P.-G. (1985). *Reviews of modern physics*, **57**(3), 827.

Dorner, B. & Wildes, A. R. (2003). *Langmuir*, **19**(19), 7823–7828.

Durniak, C., Ganeva, M., Pospelov, G., Herck, W. V. & Wuttke, J., (2015). Bornagain - software for simulating and fitting x-ray and neutron small-angle scattering at grazing incidence. http://www.bornagainproject.org.

Fragneto, G., Delhom, R., Joly, L. & Scoppola, E. (2018). *Current opinion in colloid & interface science*, **38**, 108–121.

Geoghegan, M. & Krausch, G. (2003). *Progress in Polymer Science*, **28**(2), 261–302.

Gorkov, D., Toperverg, B. & Zabel, H. (2020). *Physical Review B*, **101**(22), 224404.

Gutfreund, P., Saerbeck, T., Gonzalez, M. A., Pellegrini, E., Laver, M., Dewhurst, C. & Cubitt, R. (2018). *Journal of Applied Crystallography*, **51**(3), 606–615.
URL: *https://doi.org/10.1107/S160057671800448X*

Hafner, A. (2019). *Full Off-Specular and Specular Reflectometry for Soft Thin Film Analysis*. Ph.D. thesis, Université libre de Bruxelles, Faculté des Sciences Physique, Bruxelles.

Heavens, O. S. (1960). *Reports on Progress in Physics*, **23**(1), 1.
URL: *http://stacks.iop.org/0034-4885/23/i=1/a=301*

Hexemer, A. & Müller-Buschbaum, P. (2015). *IUCrJ*, **2**, 106–125.

Higgins, A. M. & Jones, R. A. (2000). *Nature*, **404**(6777), 476–478.

Holỳ, V. & Baumbach, T. (1994). *Physical Review B*, **49**(15), 10668.

Holỳ, V., Kube, J., Ohli, I., Lischka, K. & Plotz, W. (1993). *Physical Review B*, **47**, 15896–15903.
URL: *http://link.aps.org/doi/10.1103/PhysRevB.47.15896*

Jablin, M. S., Zhernenkov, M., Toperverg, B. P., Dubey, M., Smith, H. L., Vidyasagar, A., Toomey, R., Hurd, A. J. & Majewski, J. (2011). *Physical Review Letters*, **106**, 138101.
URL: *http://link.aps.org/doi/10.1103/PhysRevLett.106.138101*

Jacobs, K., Herminghaus, S. & Mecke, K. R. (1998). *Langmuir*, **14**(4), 965–969.
URL: *https://doi.org/10.1021/la970954b*

James, D., Higgins, A. M., Rees, P., Geoghegan, M., Brown, M. R., Chang, S.-S., Môn, D., Cubitt, R., Dalgliesh, R. & Gutfreund, P. (2015). *Soft matter*, **11**(48), 9393–9403.

Krivoglaz, M. A. (1969). *Theory of X-Ray and Thermal Neutron Scattering by Real Crystals.* Nauka.

Landau, L. D. & Lifshitz, E. M. (1989). *Non-Relativistic Quantum Mechanics*, vol. 3 of *Theoretical Physics*. Pergamon Press, 4th ed.

Lauter, V., Lauter, H., Glavic, A. & Toperverg, B., (2016). Reference module in materials science and materials engineering.

Lauter-Pasyuk, V., Lauter, H. J., Gordeev, G. P., Müller-Buschbaum, P., Toperverg, B. P., Jernenkov, M. & W, P. (2003). *Langmuir*, **19**(19), 7783–7788.

Liesche, G. (2012). *Flow behaviour of polymer melts and solutions at the solid-liquid interface.* Bachelor's thesis, Hochschule Bremerhaven.

Maleev, S. V. & Toperverg, B. P. (1980). *Sov. Phys. JETP*, **51**(1), 158–165.

Mandelbrot, B. B., Passoja, D. E. & Paullay, A. J. (1984). *Nature*, **308**(5961), 721–722.

Mott, N. F. & Massey, H. S. W. (1949). *The theory of atomic collisions, by Mott, NF; Massey, Harrie Stewart Wilson. Oxford, Clarendon Press, 1949.* .

Nevot, L. & Croce, P. (1980). *Revue de Physique Appliquée*, **15**(3), 761–779.

Newton, R. G. (2013). *Scattering theory of waves and particles.* Springer Science & Business Media.

Parratt, L. (1954). *Physical Review*, **95**(2), 359–369.

Penfold, J., Richardson, R. M., Zarbakhsh, A., Webster, J. R. P., Bucknall, D. G., Rennie, A. R., Jones, R. A. L., Cosgrove, T., Thomas, R. K., Higgins, J. S., Fletcher, P. D. I., Dickinson, E., Roser, S. J., McLure, I. A., Hillman, A. R., Richards, R. W., Staples, E. J., Burgess, A. N., Simister, E. A. & White, J. W. (1997). *Journal of the Chemical Society - Faraday Transactions*, **93**, 3899–3917.
URL: *http://dx.doi.org/10.1039/A702836I*

Pototsky, A., Bestehorn, M., Merkt, D. & Thiele, U. (2005). *The Journal of chemical physics*, **122**(22), 224711.

Reiter, G. (1992). *Phys. Rev. Lett.* **68**, 75–78.
URL: *https://link.aps.org/doi/10.1103/PhysRevLett.68.75*

Reiter, G., Sharma, A., Casoli, A., David, M.-O., Khanna, R. & Auroy, P. (1999). *Langmuir*, **15**(7), 2551–2558.

Richard, D., Ferrand, M. & Kearley, G. (1996). *Journal of Neutron Research*, **4**(1-4), 33–39.

Richardson, H., Carelli, C., Keddie, J. & Sferrazza, M. (2003). *The European Physical Journal E*, **12**(3), 437–441.

Runov, V. V., Ginzburg, S. L., Toperverg, B. P., Tret'yakov, A. D., Okorokov, A. I. & Mal'tsev, E. I. (1991). *Sov. Phys. JETP*, **67**(1), 181–192.

Saerbeck, T., Cubitt, R., Wildes, A., Manzin, G., Andersen, K. H. & Gutfreund, P. (2018). *Journal of Applied Crystallography*, **51**(2), 249–256.
URL: *https://doi.org/10.1107/S160057671800239X*

Seemann, R., Herminghaus, S. & Jacobs, K. (2001*a*). *Physical Review Letters*, **86**(24), 5534.

Seemann, R., Herminghaus, S. & Jacobs, K. (2001*b*). *Journal of Physics: Condensed Matter*, **13**(21), 4925.

Sferrazza, M., Heppenstall-Butler, M., Cubitt, R., Bucknall, D., Webster, J. & Jones, R. A. L. (1998). *Physical Review Letters*, **81**, 5173–5176.
URL: *http://link.aps.org/doi/10.1103/PhysRevLett.81.5173*

Sferrazza, M., Xiao, C., Jones, R. A. L., Bucknall, D. G., Webster, J. & Penfold, J. (1997). *Phys. Rev. Lett.* **78**, 3693–3696.
URL: *https://link.aps.org/doi/10.1103/PhysRevLett.78.3693*

Sharma, A. & Reiter, G. (1996). *Journal of Colloid and Interface Science*, **178**(2), 383–399.

de Silva, J. P., Cousin, F., Wildes, A. R., Geoghegan, M. & Sferrazza, M. (2012). *Phys. Rev. E*, **86**, 032801.
URL: *https://link.aps.org/doi/10.1103/PhysRevE.86.032801*

de Silva, J. P., Geoghegan, M., Higgins, A. M., Krausch, G., David, M.-O. & Reiter, G. (2007). *Phys. Rev. Lett.* **98**, 267802.
URL: *https://link.aps.org/doi/10.1103/PhysRevLett.98.267802*

de Silva, J. P., Martin, S. J., Cubitt, R. & Geoghegan, M. (2009). *Europhysics Letters*, **86**(3), 36005.
URL: *http://stacks.iop.org/0295-5075/86/i=3/a=36005*

Sinha, S. K., Sirota, E. B., Garoff, S. & Stanley, H. B. (1988). *Physical Review B*, **38**, 2297–2311.
URL: *http://link.aps.org/doi/10.1103/PhysRevB.38.2297*

Theis-Bröhl, K., Mishra, D., Toperverg, B. P., Zabel, H., Vogel, B., Regtmeier, A. & Hütten, A. (2011). *Journal of Applied Physics*, **110**(10), 102207.

Theis-Bröhl, K., Wolff, M., Ennen, I., Dewhurst, C. D., Hütten, A. & Toperverg, B. P. (2008). *Physical Review B*, **78**(13), 134426.

Tolan, M. (1998). *X-Ray Scattering from Soft-Matter Thin Films, -Materials Science & Basic Research -, STMP*. Springer.

Toperverg, B., Schärpf, O. & Anderson, I. S. (2000). *Physica B: Condensed Matter*, **276**, 954–955.

Toperverg, B. P. (2015). *The Physics of Metals and Metallography*, **116**(13), 1337–1375.

Toperverg, B. P. & Zabel, H. (2015). In *Experimental Methods in the Physical Sciences*, vol. 48, pp. 339–434. Elsevier.

Wolff, M., Devishvili, A., Dura, J. A., Adlmann, F. A., Kitchen, B., Pálsson, G. K., Palonen, H., Maranville, B. B., Majkrzak, C. F. & Toperverg, B. P. (2019). *Phys. Rev. Lett.* **123**, 016101.
URL: *https://link.aps.org/doi/10.1103/PhysRevLett.123.016101*

Xie, R., Karim, A., Douglas, J. F., Han, C. C. & Weiss, R. A. (1998). *Physical Review Letters*, **81**(6), 1251.

Yoneda, Y. (1963). *Phys. Rev.* **131**(5), 2010.

Zabel, H., Theis-Bröhl, K. & Toperverg, B. P. (2007). *Novel Techniques for Characterizing and Preparing Samples*, vol. 3 of *Handbook of Magnetism and Advanced Magnetic Materials*, chap. Polarized Neutron Reflectivity and Scattering from Magnetic Nanostructures and Spintronic Materials, p. 1237. Hoboken: John Wiley & Sons.

Synopsis

A combined specular and off-specular neutron reflectometry analysis algorithm in absolute scale is presented. Experimental data from thermally annealed immiscible polymer bilayer systems is fitted.